*J. Fluid Mech.* (2024), *vol*. 988, A50, doi:10.1017/jfm.2024.445

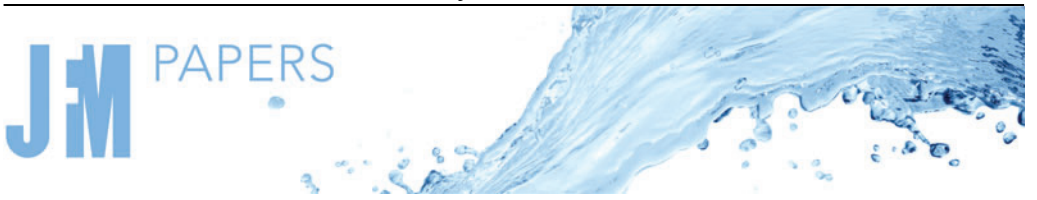


# Intrinsic features of flow-induced stability of a square cylinder

**Cuiting Lin**[1] **and Md. Mahbub Alam**[1],†

[1]Center for Turbulence Control, Harbin Institute of Technology (Shenzhen), Shenzhen 518055, China

(Received 2 October 2023; revised 23 March 2024; accepted 29 April 2024)

Vortex-induced vibrations and galloping of an elastically mounted square cylinder are investigated for cylinder mass ratio $m^* = 2$–$50$, damping ratio $\zeta = 0$–$1.0$, mass-damping ratio $m^*\zeta = 0$–$50$ and flow reduced velocity $U_r = 1$–$80$. We home in on the effects of $m^*$, $\zeta$, $m^*\zeta$, $(m^* + m^*_{a0})\zeta$ and $(m^* + m^*_{ae})\zeta$ on the critical reduced velocity $U_{rc}$ marking the onset of galloping, where $m^*_{a0}$ is the quiescent-fluid added mass ratio and $m^*_{ae}$ is the effective added mass ratio. Vibration responses, forces, vibration frequencies and added mass ratios are studied and discussed. The different branches of vortex-induced vibrations have different dependencies of $m^*_{ae}$ on $U_r$. The $m^*_{ae}$ in the initial branch is positive and drops rapidly with $U_r$, but that in the lower branch is negative and declines gently. In the galloping regime, $m^*_{ae}$ jumps from negative to positive at the onset of galloping, declining slightly with increasing $U_r$. Our results and prediction equations show that when $\zeta = 0$, $U_{rc}$ is independent of $m^*$ for $m^* \geq 5$, albeit slightly higher for $m^* = 3$. The latter is ascribed to mode competition. When $\zeta > 0$, $U_{rc}$ linearly increases with increasing $\zeta$. Detailed analysis substantiates that $m^*\zeta$ or $(m^* + m^*_{a0})\zeta$ does not serve as the unique criterion to predict the galloping occurrence. Here, we propose a new combined mass-damping parameter $(m^* + m^*_{ae})\zeta$ in the relationship between galloping onsets and structural properties, which successfully scales all data of $U_{rc}$ at different $m^*$ and $\zeta$ values.

**Key words:** flow–structure interactions, vortex shedding

## 1. Introduction

Flow-induced vibration (FIV) of slender structures is a result of fluid–structure interactions, which can be observed in many engineering fields, such as offshore drilling platforms and suspension bridges. When fluid flow passes these slender structures, they may undergo vortex-induced vibration (VIV) and/or galloping, both of which are commonly known as FIV. Blevins (1990) defined galloping as a large-amplitude and

† Email address for correspondence: alam@hit.edu.cn, alamm28@yahoo.com

low-frequency self-excited vibration of non-circular structures at a reduced velocity higher than a threshold. The galloping vibration is initiated when the overall damping of the system is negative because of negative flow-induced damping, given that the structural damping is positive (Blevins 1990; Païdoussis, Price & Delangre 2010; Qin, Alam & Zhou 2017, 2019).

Structural mass ratio $m^*$, damping ratio $\zeta$, natural frequency $f_n$, Reynolds number $Re$, reduced velocity $U_r$, structure shape and turbulent intensity all play important roles in galloping. Barrero-Gil, Sanz-Andres & Roura (2009) concluded that a square cylinder cannot gallop at $Re < 159$ with $m^*\zeta = 0.25$, 1.25 and 2.5, while Joly, Etienne & Pelletier (2012) observed galloping for $Re > 140$ with $m^* = 20$, $\zeta = 0$. The latter threshold $Re$ value is much lower than the former. When $Re$ was systematically increased with $m^* = 10$, $\zeta = 0$, Sen & Mittal (2011) found that the oscillation frequency abruptly decreases at $Re > 170$ when a square cylinder vibrates in both transverse and streamwise directions, which points to the occurrence of galloping instability. The galloping vibration regime ($Re > 170$) corresponded to 2S (two single vortices in one oscillation period) and 2P (two paired vortices) vortex shedding modes. The 2S and 2P modes were associated with high-amplitude ($Re < 215$) and very-high-amplitude ($Re \geq 215$) vibrations, respectively. At $Re \geq 220$, the transverse vibration amplitude when the cylinder was only allowed to vibrate in the transverse direction was much smaller than that when it was allowed to vibrate in both transverse and streamwise directions. For the transverse vibration, the 2S mode prevailed. Sen & Mittal (2015) investigated the influence of $m^*$ on galloping instability for $m^* = 1$, 5, 10 and 20, $\zeta = 0$ and $Re = 50$–$250$. Galloping was only found for high $m^* = 5$, 10 and 20 with the onset of galloping at $Re = 186$, 174 and 169, respectively. With increasing $m^*$, the critical $Re$ (or critical reduced velocity $U_{rc}$) marking the onset of lock-in and galloping increases and decreases, respectively. They varied $U_r$ by increasing the free-stream flow velocity (i.e. $Re$), where the Strouhal number and forces of a fixed cylinder are very sensitive to $Re$. Given that they increased $U_r$ by varying $Re$, their $m^*$ effect is contaminated by the $Re$ effect, as is shown later. They identified three vortex-shedding modes: 2S, C(2S) and 2P + 2S. Modes 2S and C(2S) are involved in VIV, whereas the galloping vibration features 2S mode for $A^*$ ($= A/D$) $< 0.7$ and 2P + 2S mode for $A^* > 0.7$, where $A$ is the vibration amplitude and $D$ is the cylinder width.

For a square cylinder with $m^* = 10$, Bhatt & Alam (2018) reported the occurrence of galloping at $Re = 200$ but not at $Re = 100$. In the case of galloping vibrations, they observed N(2S) vortex shedding mode, where the wake is akin to the wake of a 2S mode. Zhao (2015) examined the FIVs of a square cylinder and a rectangular cylinder at $m^* = 10$, $Re = 200$, and found that $U_{rc}$ for galloping increases with increasing cylinder cross-sectional aspect ratio $\alpha$, with $U_{rc} = 13$ for the square cylinder. Zhao *et al.* (2019) experimentally investigated the effect of $m^*$ on the vibration response of a square cylinder at $\zeta = (1.31$–$2.58) \times 10^{-3}$. When $m^*$ was increased, the combined VIV–galloping response weakened and ceased to exist for $m^* \geq 11.31$. Sourav & Sen (2019) for $Re \leq 250$ identified the threshold $m^* = 3.4$ above which VIV and galloping were separated. Han & Langre (2022) at low Reynolds numbers pointed out that galloping may occur even for a very low mass ratio, and there is no critical mass ratio for galloping of a square cylinder. The galloping onset is delayed at a low mass ratio.

The effects of $m^*$, $\zeta$ and $m^*\zeta$ on the response of a freely vibrating circular cylinder were numerically investigated by Bahmani & Akbari (2010) for $Re = 80$–$160$. When $m^*$ or $\zeta$ was increased, both $A^*$ and $U_r$ ranges of VIV shrank. They further noted that the oscillator system behaves nonlinearly with $m^*$ and $\zeta$. Rabiee & Farahani (2020) numerically investigated FIV of a heated square cylinder with $\zeta = 0$, 0.01, 0.05, 0.1, 0.25

and 0.5 at $Re = 80$, 90, 220 and 250. They also observed an inverse relationship between $A^*$ and $\zeta$. At $Re = 220$ involving galloping vibrations, as $\zeta$ increases from 0 to 0.1 and 0.25, $A^*$ reduces by 36 % and 91 %, respectively.

As $Re$, $U_r$, $m^*$ and $\zeta$ all play key roles in vibration generation, they all must simultaneously exceed their threshold values for the onset of galloping. In general, if any of these parameters falls short of the corresponding threshold value with the remaining parameters being sufficiently high, the cylinder will execute VIV alone, and the transition to galloping will not take place.

Sen & Mittal (2016) found that the wake mode type is a direct function of the synchronization type; it is a 2S or C(2S) mode for 1:1 synchronization between the oscillation and shedding frequencies, a 2P + 2S mode when the synchronization is very close or equal to 1:3 and a 3(2S) or unstable 2S mode when the synchronization is a little far from 1:3. Zhao *et al*. (2014) experimentally observed an increased $A^*$ for 1:3 synchronization, deviating from the trend of the typical galloping response. Yao & Jaiman (2017) found a low-frequency galloping instability and a kink in the amplitude response around 1:3 synchronization for a triangular cylinder. Daniel, Todd & Yahya (2021) observed amplitude deviations from a typical galloping response at higher synchronizations.

Beating phenomena in instantaneous vibration responses were observed in some studies on VIV of a circular cylinder. Khalak & Williamson (1999) indicated that this beating is associated with the transition between the lower and upper branches, and hence between the 2S and 2P modes. Voorhees *et al*. (2008) pointed out that the difference in frequencies between the cylinder vibration and the vortex shedding gives rise to the beating. Shen, Chan & Wei (2018) reported similar observations. The modulation frequency equals the difference between the two frequencies. In the galloping branch, the vibration of a square cylinder is generally quasi-periodic, but it is periodic only when the vortex-shedding to oscillation frequency ratio $f_s/f_o = 3$ (Zhao *et al*. 2014; Zhao 2015; Sen & Mittal 2016). We focus on not only the effect of $m^*$ but also $\zeta$ and a combined mass-damping parameter on the vibration responses of a square cylinder, and revisit the mechanisms and roles of the 1:3 and 1:5 synchronizations further.

### 1.1. *Objective*

The transverse dynamic response of a cylinder can be simplified as a spring–damper–mass system expressed in non-dimensional form as

$$\ddot{Y} + 4\pi \left(\frac{1}{U_r}\right) \zeta \dot{Y} + \left(\frac{2\pi}{U_r}\right)^2 Y = \frac{C_L}{2m^*}, \tag{1.1}$$

where $Y$, $\dot{Y}$ and $\ddot{Y}$ are respectively the instantaneous displacement, velocity and acceleration of the cylinder in the transverse direction. The non-dimensional parameters are defined and listed in table 1, where $c$ and $k$ are the damping and spring constants of the cylinder system, respectively. Parameter $m$ is the mass of the cylinder per unit length and $\rho$ is the density of the fluid. Terms $f_o$ and $f_s$ are the cylinder vibration frequency and vortex shedding frequency, respectively. Force $F_L$ is the lift force acting on the unit span of the cylinder.

In (1.1), $U_r$, $\zeta$ and $m^*$ are the parameters involved in FIVs while $C_L$ is the flow-induced lift force that depends on $U_r$, $\zeta$, $m^*$ and $Y$. One can estimate $C_L$ from (1.1) when $U_r$, $\zeta$, $m^*$ and $Y$ are all known. Undoubtedly, $\zeta$ and $m^*$ are the structural parameters, the latter

| | |
|---|---|
| Amplitude ratio: $A^* = A/D$ | Lift force coefficient: $C_L = F_L/(0.5\rho DU_\infty^2)$ |
| Reduced velocity: $U_r = U_\infty/(f_n D)$ | Normalized time: $t^* = tU_\infty/D$ |
| Mass ratio: $m^* = m/(\rho D^2)$ | Normalized pressure: $p^* = p/(\rho U_\infty^2)$ |
| Damping ratio: $\zeta = c/(2\sqrt{km})$ | Frequency ratio: $f_r = f_o/f_n$ |
| Natural frequency: $f_n = 1/2\pi\sqrt{k/m}$ | Reynolds number: $Re = \rho U_\infty D/\mu$ |
| Strouhal number: $St = f_s D/U_\infty$ | Critical damping: $c_c = 4\pi m f_n$ |

Table 1. Definitions of non-dimensional parameters.

indicating the heaviness of the structure. On the other hand, $U_r$ ($= U_\infty/f_n D$, as defined in table 1), consists of a structural parameter (i.e. $f_n$) and a flow parameter (i.e. $U_\infty/D$), the former representing the structural rigidity or strength (how many oscillations per second) while the latter indicating the flow strength (how many $D$ the flow can travel per second) or forcing frequency in other words. Thus, $U_r$ represents a competition between the structural rigidity and flow strength. That is, the smaller the $U_r$, the higher the structural rigidity and/or the smaller the flow strength, and *vice versa*. If $U_r$ with a constant $f_n D$ is varied by changing $U_\infty$ (i.e. $Re$), it acts as a flow parameter. Conversely, if $U_r$ is varied via $f_n$, keeping $U_\infty$ (i.e. $Re$) constant, it acts as a structural parameter. When the effect of $U_r$ on $A^*$ (i.e. $A^*$ versus $U_r$ graph) is investigated with increasing $U_r$ via $U_\infty$, the effect involves the combined influence of $U_r$ and $Re$. On the other hand, when the same is done via $f_n$, it solely involves the influence of $U_r$. When $Re$ is kept constant, a better presentation of the $U_r$ effect is provided.

We aim to investigate the effects of $m^*$ ($= 2$–$50$), $\zeta$ ($= 0$–$1$), $m^*\zeta$ ($= 0$–$50$) and $U_r$ ($= 1$–$80$) on vibration and frequency responses, flow structures, added mass and forces of an elastically mounted square cylinder at $Re = 170$. This investigation further explores whether $m^*\zeta$ is an appropriate parameter to characterize FIV. If not, what is the appropriate parameter? To guarantee the occurrence of galloping and avoid the three-dimensional effect, we select $Re = 170$ based on investigations by Barrero-Gil *et al.* (2009), Joly *et al.* (2012) and Sen & Mittal (2011).

## 2. Methodology

### 2.1. *Governing equations and numerical set-up*

The flow is assumed to be incompressible, viscid and two-dimensional while the physical properties of the fluid are constant. The governing equations to simulate the flow field around an elastically mounted rigid square cylinder are the continuity and Navier–Stokes equations, which can be written in a non-dimensional form as

$$\text{continuity:} \quad \nabla \boldsymbol{u}^* = 0 \tag{2.1}$$

and

$$\text{momentum:} \quad \frac{\partial \boldsymbol{u}^*}{\partial t^*} + \boldsymbol{u}^* \nabla \boldsymbol{u}^* = -\nabla p^* + \frac{1}{Re}\nabla^2 \boldsymbol{u}^*, \tag{2.2}$$

where $p^*$ ($= p/\rho U_\infty^2$), $\boldsymbol{u}^*$ and $t^*$ ($= tU_\infty/D$) are the normalized static pressure, normalized velocity and normalized time, respectively. Term $\boldsymbol{u}^*$ is composed of two velocity components $\boldsymbol{u}^* = (u^*, v^*) = (u/U_\infty, v/U_\infty)$ in the streamwise and transverse directions, respectively. Parameter $D$ is the width of the square cylinder. Reynolds number is defined as $Re = \rho U_\infty D/\mu$, where $\mu$ is the viscosity of the fluid, $\rho$ is the fluid density and $U_\infty$ is the

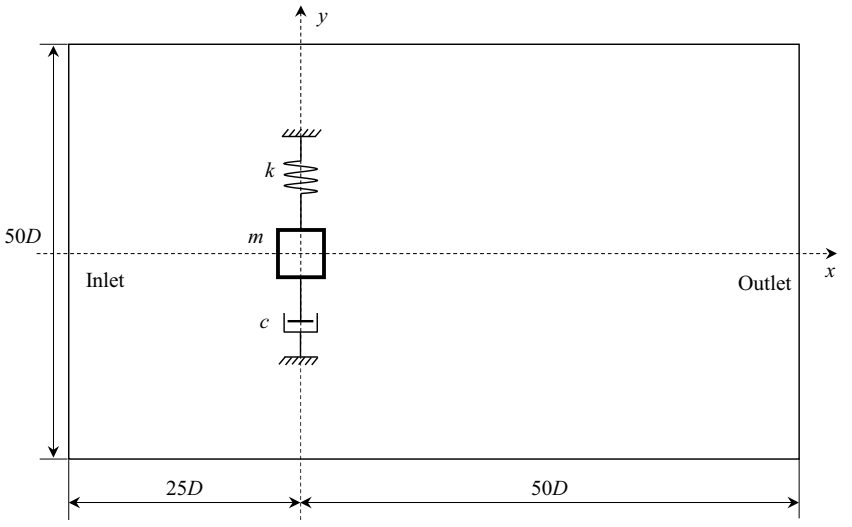


Figure 1. A schematic of the flow configuration and computational domain.

free-stream flow velocity. The reduced velocity $U_r = U_\infty/(f_n D)$, where $f_n$ $(= 1/2\pi\sqrt{k/m})$ is the natural frequency of the cylinder.

Ansys-Fluent 17.2 based on the finite-volume method is utilized as the solver. The second-order upwind scheme and the central differencing scheme are used to discretize the convective and diffusion terms, respectively. A first-order implicit formulation is adopted for time discretization because of its unconditional stability (Manson, Pender & Wallis 1996) and compatibility with the dynamic mesh (Shaaban & Mohany 2018). The pressure-correction-based iterative algorithm SIMPLE (semi-implicit method for pressure-linked equations) proposed by Patankar (1980) is employed for coupling the velocity and pressure fields.

The dynamic response of the cylinder system is given by (1.1). The fourth-order Runge–Kutta method is employed to solve this second-order differential equation at each time step, where the fluid forces acting on the cylinder are composed of pressure and shear stress forces, obtained directly from the ANSYS-Fluent 17.2 solver. The lift force is provided on the right-hand side of (1.1), which is integrated to advance the cylinder motion. In the next time step, the cylinder displacement, velocity and acceleration are updated, and the equation of fluid motion is integrated to complete the fluid–solid coupling. At each time step, the deformation of the computational domain is managed by the dynamic meshing tool in ANSYS-Fluent 17.2, with the mesh updated using the Laplace smoothing and layering methods. In the subsequent time step, the field variables ($u$, $v$ and $p$) within the entire computational domain are updated based on each node's information, which involves solving the governing equations: the continuity (2.1) and the Navier–Stokes (2.2) equations.

### 2.2. *Domain size, grid resolution and time-step dependence test*

A schematic of the cylinder configuration is shown in figure 1. The computational domain is rectangular, scaled with $D$ as a length of $L_u + L_d = 75D$ in the flow direction and a height of $H = 50D$ in the transverse direction. It gives a blockage ratio $D/H = 2.0\,\%$, which is less than the 3.3 % used in Zheng & Alam (2017) and Bhatt & Alam (2018). The boundary

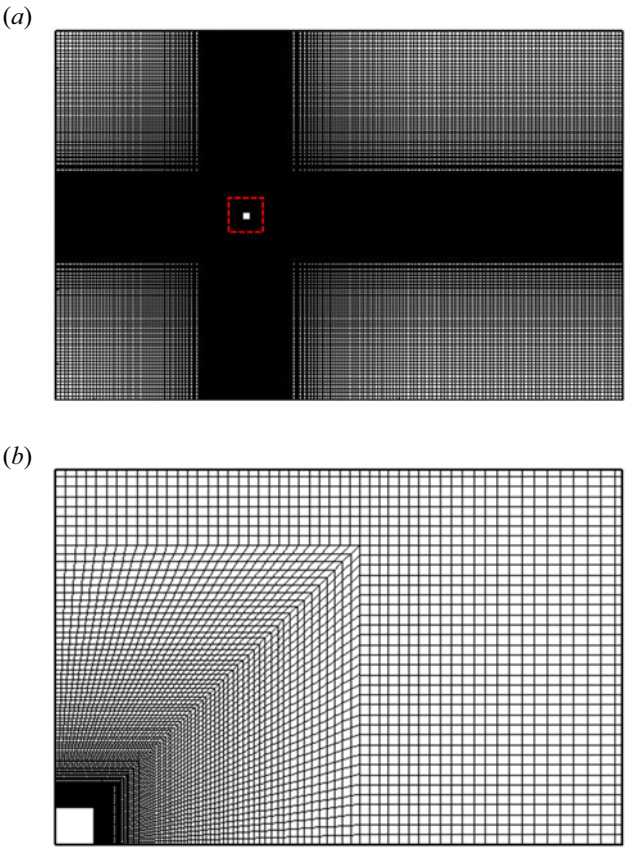


Figure 2. (*a*) Global view and (*b*) zoomed-in view of the meshes around the square cylinder.

conditions at the inlet are $u^* = 1.0$, $v^* = 0$. Symmetry conditions ($v^* = 0$, $\partial u^*/\partial y^* = 0$ and $\partial p^*/\partial y^* = 0$) are applied to both upper and lower boundaries. The inlet boundary is set as the velocity inlet ($u^* = 1$, $v^* = 0$), while the outlet boundary is given as $\partial u^*/\partial x^* = 0$, $\partial v^*/\partial x^* = 0$ and $\partial p^*/\partial x^* = 0$. No-slip boundary conditions are deployed on the cylinder surface. The initial flow field in the computation domain is given as $u^* = 1$, $v^* = 0$ and $p^* = 0$.

Figure 2(*a*) shows a global view of grid distributions in the entire computational domain, and figure 2(*b*) shows a zoom-in view of grid distributions around a quadrant of the square cylinder. The entire flow field is given a structured quadrangular grid system. The oscillating cylinder is surrounded by a central box of size $8D \times 8D$ (figure 2*a*). The central box of high grid density moves with the vibrating cylinder, while the remaining grids in the domain are stationary. A dynamic mesh scheme is utilized to move the cylinder including the central box and to adjust the mesh accordingly. The motion of the cylinder is defined by the user-defined function. At each time step, smoothing and layering are applied at each new position of the cylinder.

Grid and time-step independence tests were performed for a vibrating cylinder with $m^* = 10$ and $U_r = 7$ (table 2). Four grids M1 = 22 292, M2 = 44 799, M3 = 76 622 and M4 = 145 232 were tested, each with time steps $\Delta t = 0.001$, 0.002, and 0.005. The values of $A^*$, $f_r = f_o/f_n$ and $C_L'$ are presented in table 2, where $f_o$ was estimated from the fast Fourier transform (FFT) of the $Y$ signal, $A^*$ was obtained from the root-mean-square value

| $\Delta t$ (s) | Number of nodes | $A^*$ | $f_r$ | $C_L'$ |
|---|---|---|---|---|
| 0.005 | 22 292 (M1) | 0.0829 (21.11 %) | 1.0838 (3.87 %) | 0.1603 (27.14 %) |
| | 44 799 (M2) | 0.0654 (9.17 %) | 1.1258 (2.65 %) | 0.2038 (3.39 %) |
| | 76 622 (M3) | 0.0594 (4.71 %) | 1.1556 (0.32 %) | 0.2107 (0.95 %) |
| | 145 232 (M4) | 0.0566 | 1.1594 | 0.2127 |
| 0.002 | 22 292 (M1) | 0.0833 (21.85 %) | 1.0996 (4.49 %) | 0.1905 (23.52 %) |
| | 44 799 (M2) | 0.0651 (8.60 %) | 1.149 (1.61 %) | 0.2353 (3.02 %) |
| | 76 622 (M3) | 0.0595 (3.87 %) | 1.1675 (0.27 %) | 0.2424 (0.04 %) |
| | 145 232 (M4) | 0.0572 | 1.1643 | 0.2423 |
| 0.001 | 22 292 (M1) | 0.0853 (22.74 %) | 1.0823 (6.67 %) | 0.1939 (26.87 %) |
| | 44 799 (M2) | 0.0659 (9.41 %) | 1.1545 (0.95 %) | 0.246 (2.97 %) |
| | 76 622 (M3) | 0.0597 (3.52 %) | 1.1654 (0.25 %) | 0.2533 (0.04 %) |
| | 145 232 (M4) | 0.0576 | 1.1625 | 0.2534 |

Table 2. Grid and time-step independence tests for vibrating cylinder at $Re = 170$, $m^* = 10$ and $U_r = 7$.

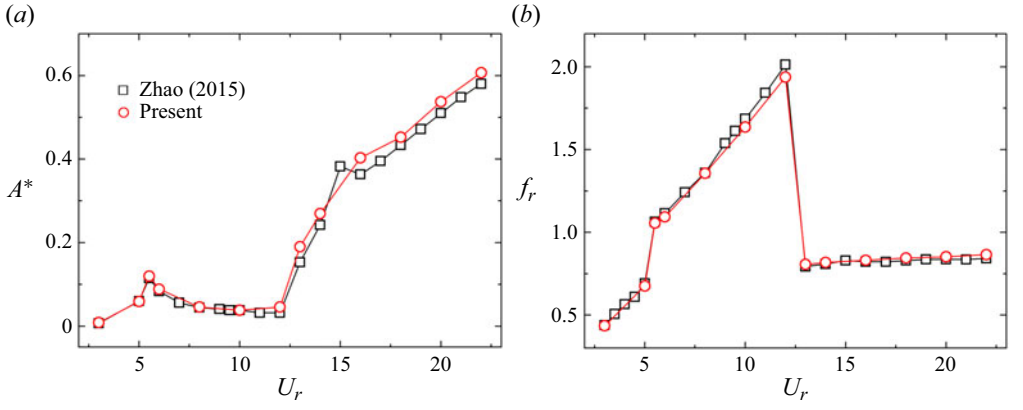


Figure 3. Comparisons of (*a*) response amplitude $A^*$ and (*b*) frequency ratio $f_r$ ($=f_o/f_n$) of a square cylinder at mass ratio $m^* = 10$, damping ratio $\zeta = 0$ for $Re = 200$.

of $Y$ as $A^* = Y_{rms} \times \sqrt{2}/D$ and $C_L'$ was calculated from the lift signal. The percentage deviation is provided in parentheses with increasing node numbers. When the grid system increases from M1 to M4, the deviations get smaller. The deviations in the results between M3 and M4 for $\Delta t = 0.001$, 0.002 and 0.005 are less than 3.52 %, 3.87 % and 4.71 %, respectively. Grid M3 is considered, given that the node number for M4 is approximately twice that for M3 and the deviations in the results between M4 and M3 are small. The deviations in the results for M3 are less than 4.3 % between $\Delta t = 0.002$ and 0.001, while it is 13.08 % between $\Delta t = 0.005$ and 0.002. Grid M3 and $\Delta t = 0.002$ are thus chosen for further successive simulations. There were 240 nodes on each side of the cylinder surface for M3. The first layer of elements had a radial distance of $0.005D$ from the cylinder surface.

### 2.3. *Validation*

In addition to the grid and time-step validation, the model for FIVs was validated for a square cylinder vibration at $Re = 200$ for $U_r = 3$–22. This $Re = 200$ is chosen to compare the results from Zhao (2015). Figure 3 compares the vibration and frequency responses

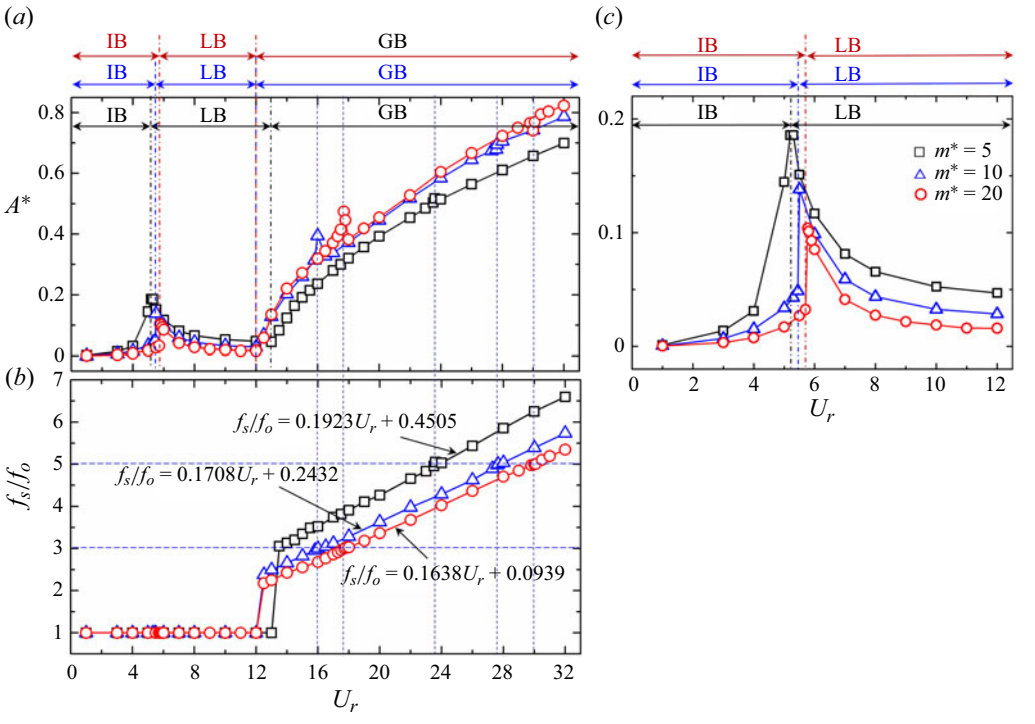


Figure 4. Dependence on reduced velocity $U_r$ and mass ratio $m^*$ of (*a*) response amplitude $A^*$ and (*b*) $f_s/f_o$. (*c*) Zoom-in view of $A^*$–$U_r$ plot in (*a*) for $U_r = 1$–12. Here, $\zeta = 0$ and $Re = 170$.

between the present and Zhao's works for a cylinder with $m^* = 10$, $\zeta = 0$, and $Re = 200$. The present results of $A^*$ and $f_r$ concur well with those of Zhao (2015).

## 3. Results and discussion

### 3.1. *Effect of m* on vibration response*

We present here the effect of $m^*$ on vibration and frequency responses at $\zeta = 0$ (figure 4). The cylinder responses can be divided into three branches, namely the initial branch (IB), lower branch (LB) and galloping branch (GB). For $m^* = 20$, the vortex excitation regime (including IB and LB) appears when $U_r \leq 12$, whereas GB occurs when $U_r > 12$. Following Bhatt & Alam (2018), the identifications of IB and LB are made based on the relationship between $St$ and $U_r$ shown in figure 5(*a*). The Strouhal number $St$ – the dimensionless vortex shedding frequency of the vibrating cylinder – was estimated from the power spectral density functions of the lift signals. Here, $St_0$ is used to denote the dimensionless shedding frequency of a fixed cylinder (figure 5*a*). The IB corresponds to $St < St_0$ while the LB to $St > St_0$. The boundary between IB and LB is characterized by a jump in $St$, e.g. between $U_r = 5.7$ and 5.77 for $m^* = 20$, between $U_r = 5.45$ and 5.5 for $m^* = 10$ and between $U_r = 5.2$ and 5.3 for $m^* = 5$ (figure 5*a*). The value of $A^*$ increases with increasing $U_r$ in IB, which is accompanied by a declining $St$ and a constant $f_s/f_o = 1.0$ (figures 4*a*,*b* and 5*a*). The $f_s/f_o = 1.0$ indicates the lock-in (figure 4*b*). On the other hand, $f_r$ grows with increasing $U_r$ (figure 5*b*).

A marked rise in $A^*$ also characterizes the boundary between IB and LB (figure 4*c*). In the LB regime, $A^*$ after reaching a peak declines with increasing $U_r$. The LB is further

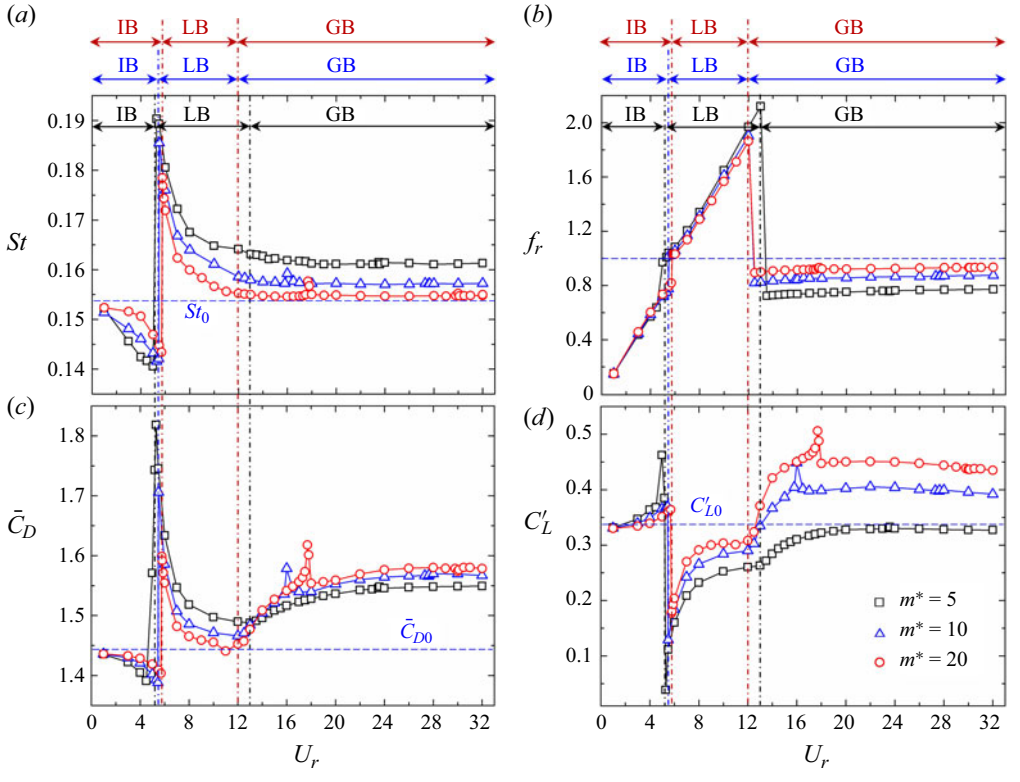


Figure 5. Variations of (*a*) Strouhal number *St*, (*b*) oscillation frequency ratio $f_r$, (*c*) time-mean drag coefficient $\bar{C}_D$ and (*d*) fluctuating lift $C'_L$ with reduced velocity $U_r$ for different mass ratio $m^*$ values. Here, damping ratio $\zeta = 0$ and $Re = 170$.

characterized by $f_s/f_o = 1.0$ (lock-in, figure 4*b*), declining *St* and increasing $f_r$. These three attributes are similar to those in IB. How do IB and LB differ? Why are there jumps in *St* and $f_r$ between IB and LB? The distinct phase lag $\phi$ between $C_L$ and $Y^*$ ($= Y/D$) answers these two questions: $\phi = 0°$ in IB and $\phi = 180°$ in LB (not shown), given $\zeta = 0$. The jump in $\phi$ from 0° to 180° occurs at the boundary between IB and LB.

The GB can be identified from the recovery in the increase of $A^*$ (figure 4*a*) and jump in $f_s/f_o$ (figure 4*b*) or from the plunge in $f_r$ (figure 5*b*). Therefore, the critical reduced velocity $U_{rc}$ for the onset of galloping is 13, 12 and 12 for $m^* = 5$, 10 and 20, respectively. In GB, $A^*$ increases rapidly with $U_r$. Deviating from this trend, $A^*$ surges at 1:3 (i.e. $f_s/f_o = 3$) and 1:5 (i.e. $f_s/f_o = 5$) synchronizations (figure 4*a*,*b*). The surge is stronger at 1:3 synchronization than at 1:5 synchronization. The onset of galloping for $m^* = 5$ coincides with 1:3 synchronization. Sen & Mittal (2016), Yao & Jaiman (2017) and Daniel *et al.* (2021) all observed 1:3 synchronization. Here, we find that 1:5 synchronization also plays a role in the vibration responses. The vibration response is generally quasi-periodic (amplitude varying with time) but is periodic (constant amplitude) for 1:3 and 1:5 synchronizations. Sen & Mittal (2016) reported that the vibration response for $m^* = 5$ was quasi-periodic for the entire GB because they ignored the 1:5 synchronization.

Term $f_s/f_o$ in GB generally increases linearly with increasing $U_r$ except for the occurrence of synchronizations around $f_s/f_o = 3$ or 5 (figure 4*b*). The linear relationship

between $f_s/f_o$ and $U_r$ can be expressed as

$$f_s/f_o = 0.1638U_r + 0.0939 \quad \text{for } m^* = 20, \tag{3.1a}$$

$$f_s/f_o = 0.1708U_r + 0.2432 \quad \text{for } m^* = 10, \tag{3.1b}$$

$$f_s/f_o = 0.1923U_r + 0.4505 \quad \text{for } m^* = 5. \tag{3.1c}$$

The value of $St$ is more or less independent of $U_r$ in the galloping regime while $f_r$ being smaller than 1.0 slightly increases with $U_r$ (figure 5*a*,*b*).

Parameter $m^*$ plays a crucial role in $A^*$. It is a well-accepted argument that an increase in $m^*$ reduces $A^*$ (e.g. Bahmani & Akbari 2010). In the vortex excitation regime (including IB and LB), a larger $m^*$ leads to a smaller $A^*$ and a postponement of the $A^*$ peak. On the other hand, in the GB regime, the scenario is the opposite: the larger the value of $m^*$, the larger is $A^*$ and the smaller is $U_r$ for galloping onset (figure 4*a*). That is, the vortex excitation regime shrinks, and the onset of galloping advances when $m^*$ is increased. The surge in $A^*$ at 1:3 synchronization grows with increasing $m^*$. In addition, a larger $m^*$ in the GB regime leads to (i) reductions in $f_s/f_o$ and gradient of $f_s/f_o$ with $U_r$ (figure 4*b*; (3.1)), (ii) a decrease of $St$ and (iii) an augmentation of $f_r$.

The maximum $A^*$ of a square cylinder in the VIV regime is much smaller than that of a circular cylinder case (Sen & Mittal 2011, 2015; Li *et al*. 2019). Li *et al*. (2019) for a square cylinder at $Re = 150$ demonstrated that the maximum $A^*$ is 0.17, 0.14 and 0.11 at $m^* = 5$, 10 and 20, respectively. Zhao (2015) observed the maximum $A^*$ of 0.11 at $m^* = 10$ and $Re = 200$. The maximum $A^*$ in our study ($Re = 170$) is 0.18, 0.14 and 0.1 at $m^* = 5$, 10 and 20, respectively. Thus, the observed influence of $m^*$ on the vibration response within the VIV regime in our study appears to be consistent with the previous findings. Experimental results, typically obtained at higher $Re$ values, feature larger $A^*$ values in the galloping regime (Zhao *et al.* 2014) than the numerical results at lower $Re$ values.

### 3.2. *Effect of m* on fluid forces*

Figure 5(*c*,*d*) illustrates dependencies of $\bar{C}_D$ and $C'_L$ on $U_r$ for different $m^*$ values. The corresponding $\bar{C}_{D0}$ and $C'_{L0}$ for the fixed cylinder are represented by blue dashed lines. In IB, with increasing $U_r$, $\bar{C}_D$ ($< \bar{C}_{D0}$) declines and $C'_L$ ($> C'_{L0}$) grows for all $m^*$ values. A larger $m^*$ corresponds to a larger $\bar{C}_D$ but a smaller $C'_L$. The scenario is the opposite in LB, i.e. $\bar{C}_D > \bar{C}_{D0}$ and $C'_L < C'_{L0}$, the former declining and the latter growing. On the other hand, $\bar{C}_D$ augments in GB, with surges at 1:3 synchronization. Although rising in the early part of GB (i.e. up to 1:3 synchronization for $m^* = 10$ and 20, and 1:5 synchronization for $m^* = 5$), $C'_L$ does not appreciably vary in the late part of GB.

Parameter $m^*$ has distinct influences in different regimes. Increasing $m^*$ renders increased $\bar{C}_D$ and decreased $C'_L$ in IB but the reverse correspondence in LB. In GB, relationships of $\bar{C}_D$ and $C'_L$ with $m^*$ are straightforward, both increasing with $m^*$. A fixed cylinder, complementing $f_n = \infty$, corresponds to $U_r = 0$. Parameters $\bar{C}_D$, $C'_L$ and $St$ all approach their fixed cylinder values when $U_r$ decreases toward $U_r = 0$.

#### 3.2.1. *Quiescent fluid added-mass force and flow-induced force*

According to Lighthill (1986), the lift force ($F_L$) can be decomposed into a 'potential force' component and a 'vortex force' component, where the 'potential force' is caused by the potential added-mass force and the 'vortex force' is due to the dynamics of vorticity in the flow. Given that the fluid is viscous, Alam (2022) proposed a quiescent-fluid added-mass

force $F_{La0}$ (replacing the potential force) and a flow-induced force $F_{Lf}$ (replacing the vortex force). Naturally, the magnitude of the quiescent-fluid added-mass force differs from that of the potential force, depending on the body shapes and orientations (Chen, Alam & Zhou 2020). Alam (2022) further proved that the quiescent-fluid added-mass force must be considered to correctly estimate the flow-induced force and the phase lag between force and displacement. The total lift force is expressed as

$$F_L = F_{La0} + F_{Lf}. \tag{3.2}$$

Normalizing all forces by $(1/2\rho U_\infty^2 D)$,

$$C_L(t) = C_{La0}(t) + C_{Lf}(t). \tag{3.3}$$

Here, $C_L(t)$ is the lift force coefficient, defined as $C_L(t) = F_L(t)/(0.5\rho D U_\infty^2)$, and $F_L(t)$ is the total force on the cylinder in the $y$ direction. Coefficients $C_{La0}(t)$ and $C_{Lf}(t)$ are the instantaneous quiescent-fluid added-mass force coefficient and flow-induced force coefficient, respectively.

Force $F_{La0}(t)$ is given by

$$F_{La0}(t) = -m_{a0}\ddot{y}(t) \quad \text{(neglecting quiescent - fluid damping force)}. \tag{3.4}$$

Here, $m_{a0}$ is the quiescent-fluid added mass and is expressed as $m_{a0} = m^*_{a0} \times m_d$, where $m^*_{a0}$ is the quiescent-fluid added-mass ratio and $m_d = \rho D^2$ is the fluid mass displaced by the cylinder.

The quiescent-fluid added mass and potential added mass are the added masses measured in the quiescent fluid (still and viscid fluid) and potential fluid (inviscid, incompressible fluid), respectively. The former is generally measured numerically while the latter can be measured both numerically and experimentally by plucking the cylinder in quiescent fluid. When the damping is small, the natural frequency of the cylinder system in a vacuum can be considered as

$$f_n = \frac{1}{2\pi}\sqrt{\frac{k}{m}}. \tag{3.5}$$

When the cylinder is submerged in a fluid (e.g. water), the natural frequency of the cylinder oscillation changes because of the added mass $m_a$ generated by the fluid. The modified natural frequency $f_{nf}$ of the cylinder in a fluid can be expressed as

$$f_{nf} = \frac{1}{2\pi}\sqrt{\frac{k}{m + m_a}}. \tag{3.6}$$

Combining (3.5) and (3.6),

$$m_a = m\left[\left(\frac{f_n}{f_{nf}}\right)^2 - 1\right]. \tag{3.7}$$

When $f_{nf}$ is measured directly from the decay of the cylinder oscillation, all the parameters on the right-hand side of (3.7) are known, which leads to the estimation of $m_a$. See Chen *et al*. (2020) and Alam (2022) for details of measuring $m_a$. The quiescent-fluid added-mass coefficient $m^*_{a0}$ is coincidentally about 1.0 for a circular cylinder but approximately 1.5 for a square cylinder with zero incidence angle (Chen *et al*. 2020).

Following (3.3), $C_L(t)$ is then decomposed into $C_{La0}(t)$ and $C_{Lf}(t)$, and their corresponding fluctuating (root-mean-square) coefficients $C'_{La0}$ and $C'_{Lf}$, respectively, are

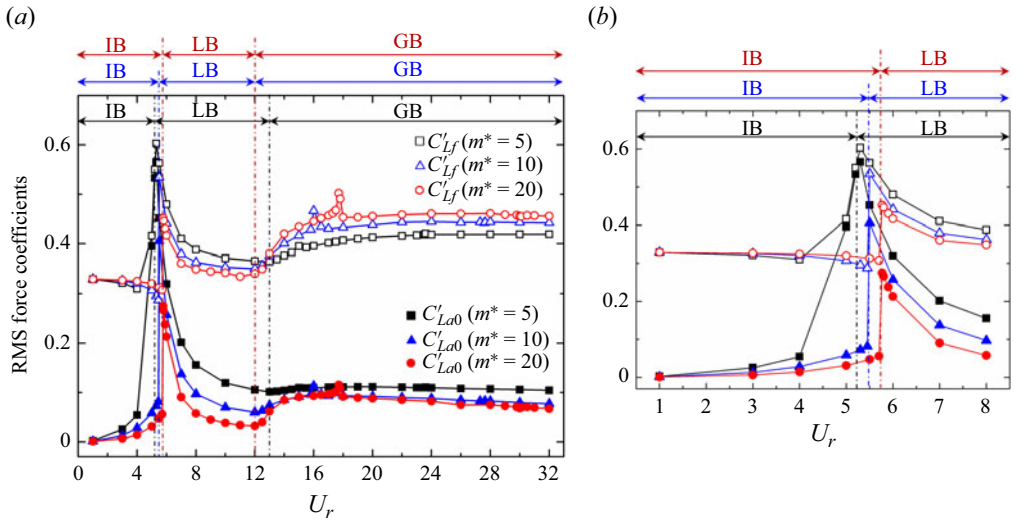


Figure 6. (*a*) Variations of fluctuating quiescent-fluid added-mass force coefficient $C'_{La0}$ and flow-induced lift coefficient $C'_{Lf}$ with $U_r$ and $m^*$. (*b*) Zoomed-in view of (*a*) for $U_r = 1$–8. Here, $\zeta = 0$ and $Re = 170$.

obtained as presented in figure 6. Coefficient $C'_{La0}$ gets smaller with increasing $m^*$ in all branches. In IB, the growth in $C'_{La0}$ is very high for all $m^*$ values, largely following $A^*$ trends in IB. On the other hand, $C'_{Lf}$ in IB does not change appreciably for the high $m^* = 10$ and 20 but does increase for the low $m^* = 5$. Both $C'_{La0}$ and $C'_{Lf}$ decline in LB for all $m^*$ values. This suggests that the increase of $A^*$ in IB is largely due to the imminent resonance effect (vortex shedding frequency approaching the cylinder natural frequency), while the decrease of $A^*$ in LB results from the decreasing $C'_{Lf}$ and the retreating resonance effect (vortex shedding frequency retreating from the cylinder natural frequency). A larger $m^*$ leads to a smaller $C'_{Lf}$ in LB but the opposite scenario takes place in GB. Interestingly, in GB, although $A^*$ increases with increasing $U_r$ for all $m^*$ values, $C'_{Lf}$ and $C'_{La0}$ gently increase and decrease ($U_r > 16$), respectively. This indicates that flow-induced force ($F_{Lf}$) and added-mass force ($F_{L0}$) in GB vary with $U_r^{2+}$ and $U_r^{2-}$, respectively. There are peaks in $C'_{Lf}$ at $U_r = 16$ and 17.7 for $m^* = 10$ and 20, respectively, where both $U_r$ values correspond to $f_s/f_o = 3$. Similar peaks are also observed for $C'_{La0}$, albeit weaker than those for $C'_{Lf}$.

### 3.3. *Role of effective added mass ratio in vibration branches*

When a square cylinder oscillates freely in the transverse direction, the effective added mass ratio $m^*_{ae}$ and added damping ratio $\zeta_a$ can be presented as

$$m^*_{ae} = \frac{m_{ae}}{\rho D^2} = \frac{F_{L0}\cos\phi}{\rho(2\pi f_o)^2 Y_0 D^2} \tag{3.8}$$

and

$$\zeta_a = \frac{c_a}{c_c} = -\frac{F_{L0}\sin\phi}{8\pi^2 m f_o f_n Y_0}. \tag{3.9}$$

The different branches of VIVs have different relationships of $m^*_{ae}$ with $U_r$ (figure 7*e*). In IB, the $F_L$ and $Y$ signals are in phase, $\cos\phi > 0$; $m^*_{ae}$ is therefore positive. On the contrary,

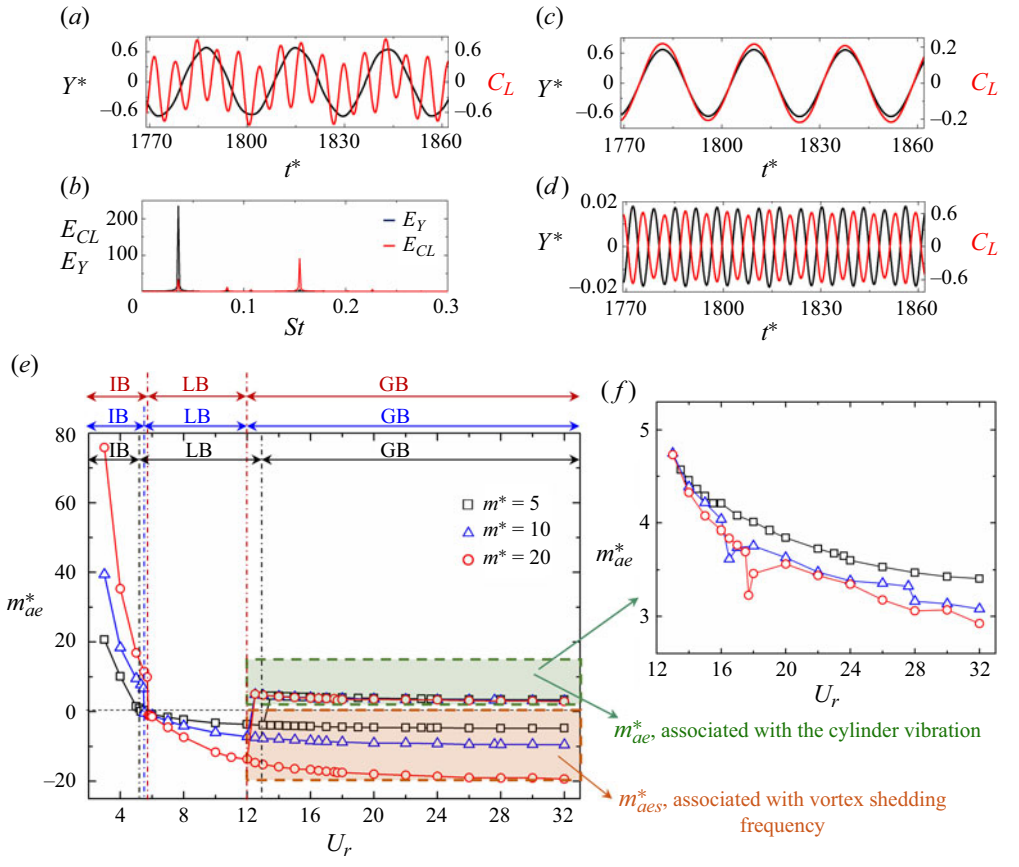


Figure 7. (*a*) Time histories, (*b*) power spectral density functions, (*c*) time histories of low-pass-filtered and (*d*) time histories of high-pass-filtered $Y^*$ (black lines) and $C_L$ (red lines) at $U_r = 26$ and $m^* = 20$. (*e*) Variations of effective added mass $m^*_{ae}$ with $U_r$ and (*f*) zoomed-in view of $m^*_{ae}$ variations in GB. Here, $\zeta = 0$ and $Re = 170$.

the $F_L$ and $Y$ signals are out of phase, $\cos\phi < 0$, in LB, which makes $m^*_{ae}$ negative. The IB and LB are distinguished by $m^*_{ae}$ changing from positive to negative (figure 7*e*). In the IB and LB, the cylinder motion is sinusoidal. The natural frequency of the vibrating cylinder is then modified because of $m_{ae}$ generated by the surrounding fluid. The modified frequency $f_{nf}$ equals the natural frequency of the cylinder vibrating in the fluid, i.e. $f_{nf} = f_o$:

$$f_o = \frac{1}{2\pi}\sqrt{\frac{k}{m + m_{ae}}}. \tag{3.10}$$

Combining (3.5) and (3.10),

$$m_{ae} = m[(f_n/f_o)^2 - 1]. \tag{3.11}$$

Parameter $m^*_{ae}$ can be presented as

$$m^*_{ae} = \frac{m_{ae}}{\rho D^2} = m^*[(f_n/f_o)^2 - 1] = m^*[(1/f_r)^2 - 1]. \tag{3.12}$$

The equation demonstrates that $m^*_{ae}$ is proportional to $[(1/f_r)^2 - 1]$. Since $f_r$ being $<1.0$ linearly grows with $U_r$ in IB (figure 5*b*), $m^*_{ae}$ being $>0$ declines parabolically with $U_r$. On the other hand, again $f_r$ grows with $U_r$ in LB but now $f_r > 1.0$, hence $m^*_{ae}$ is negative,

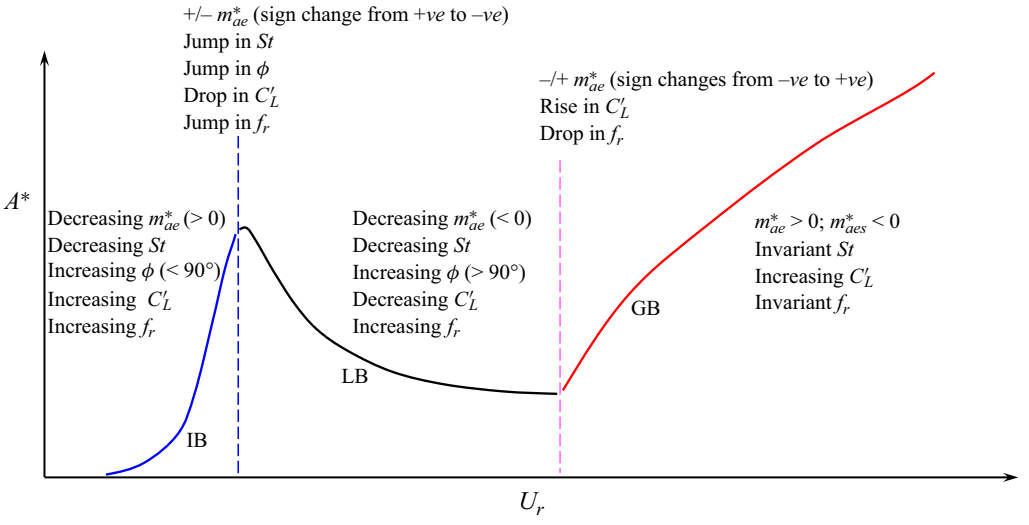


Figure 8. Typical response curve showing major characteristics in IB, LB and GB as well as at their borders.

declining with $U_r$ at a smaller slope than that in IB. A large $m^*$ yields a greater $m^*_{ae}$ magnitude in both IB and LB as $m^*_{ae}$ is directly proportional to $m^*$ (figure 7*e*; (3.12)).

In GB, both $F_L$ and $Y$ signals are composed of low- and high-frequency components corresponding to the oscillation and vortex shedding frequencies, respectively (figure 7*a*). These low- and high-frequency components were decomposed using the FFT-filter tool (figure 7*c*,*d*). The cutoff frequency for the decomposition was chosen as the average of the high and low frequencies. It can be observed that there are two major peaks in the power spectra (figure 7*b*) for the vibration in GB. The $C_L$ and $Y^*$ associated with the cylinder oscillation are in phase (figure 7*c*), while those with the vortex shedding frequency are antiphase (figure 7*d*). In GB, the effective added mass associated with the cylinder vibration can be referred to as $m^*_{ae}$ while that with the vortex shedding frequency is termed as $m^*_{aes}$ (figure 7*e*). Here $m^*_{ae}$ jumps from negative to positive at the onset of galloping. The jump in $m^*_{ae}$ is caused by the drop in $f_r$ while $m^*_{ae}$ in GB is positive because $f_r < 1.0$ (figure 5*b*; (3.12)). The value of $m^*_{ae}$ in GB slightly declines with increasing $U_r$ and $m^*$ (figure 7*f*), following the increase of $f_r$ with $U_r$ (figures 5*b* and 7*e*; (3.12)). On the other hand, $m^*_{aes}$ is negative and declines when $U_r$ is increased, and a larger $m^*$ corresponds to a smaller $m^*_{aes}$ (figure 7*e*). In IB and LB, the cylinder vortex shedding frequency ($f_s$) equals the vibration frequency ($f_o$), i.e. $f_s = f_o$, where only one frequency persists in both $F_L$ and $Y$ signals. Parameter $m^*_{aes}$ in IB and LB thus can be expressed as

$$m^*_{aes} = \frac{m_{ae}}{\rho D^2} = m^*[(f_n/f_s)^2 - 1] = m^*[(1/f_r)^2 - 1]. \tag{3.13}$$

Therefore, $m^*_{aes} = m^*_{ae}$ in IB and LB, where the dependence of $m^*_{aes}$ on $U_r$ is the same as that of $m^*_{ae}$. The major features of different branches are summarized in figure 8.

### 3.4. *Identifications of IB–LB and LB–GB boundaries*

In FIV experiments and simulations, researchers largely get vibration response ($A^*$ versus $U_r$) and have difficulty in identifying the borders between different branches in $A^*$ versus $U_r$ curves, particularly when the $A^*$ variations with $U_r$ are smooth. Bhatt & Alam (2018)

showed that the borders between IB and LB can be distinguished from the relationship between $St$ and $U_r$ as $St < St_0$ for IB and $St > St_0$ for LB. That is, the IB–LB boundary (i.e. boundary between IB and LB) is accompanied by a jump in $St$ (figure 8). Without measuring $St$, how can the borders be determined? Here are additional methods to identify the borders. Firstly, the IB–LB boundary can be identified from the change in $m^*_{ae}$ from +ve to −ve, and the LB–GB boundary can be pinpointed from the change in $m^*_{ae}$ from −ve to +ve (figures 7*e* and 8). Secondly, the IB–LB boundary is characterized by a jump in $Y^* - C_L$ phase lag from $<90°$ to $>90°$ (Williamson & Goverdhan 2004; Bhatt & Alam 2018). Thirdly, a dramatic drop and a rise in $C'_L$ mark the IB–LB and LB–GB boundaries, respectively (figures 5*d* and 8). Fourthly, the IB–LB and LB–GB boundaries undergo a jump and a drop in $f_r$, respectively. In the literature, the identification of different branches was made based on the relationship between $St$ and $U_r$. Here, we explore more avenues and generalize them to expand the methodology for identifying these branches. Figure 8 encompasses all possible parameter changes (i.e. $m^*_{ae}$, $St$, $\phi$, $C'_L$ and $f_r$), which aids in discerning distinct vibration branches when one of the parameters is measured.

### 3.5. *Beat mechanism different from the classical beat*

Next, we focus on the reasons for the uneven features of the vibration amplitude in the GB, taking the case of $m^* = 20$ and $\zeta = 0$ as an example. Except at $U_r = 17.7$–$17.8$ and $U_r = 30$–$30.1$, the vibrations in GB do not exactly repeat from one period to another (figures 9 and 10), which indicates that there are multiple frequency components, resulting in an obvious beat-like variation in the amplitudes of $Y^*$ histories. As already discussed with figure 4(*a*,*b*), $U_r = 17.7$–$17.8$ and $U_r = 30$–$30.1$ correspond to 1:3 (i.e. $f_s/f_o = 3$) and 1:5 (i.e. $f_s/f_o = 5$) synchronizations, respectively. Interestingly, the beating amplitude in $Y^*$ (i.e. the change in the vibration amplitude due to beating) grows and declines as $f_s/f_o$ respectively approaches and departs from $f_s/f_o = 3$ and/or 5, as does the beating period (figures 9 and 10). The general consensus is that a beat is characterized by amplitude modulation. It is an interference pattern between two different frequencies, perceived as a periodic variation in amplitude. As two frequencies are close to each other (i.e. small difference between them), the beating period becomes longer and it will be infinite (constant amplitude) when the two frequencies are identical.

First, we analyse the beat phenomenon for $f_s/f_o = 3$. The Lissajous diagrams of $C_L$–$Y^*$ for $U_r = 15$–$20$ presented in figure 11 also demonstrate that the vibration amplitude in GB changes from cycle to cycle except at $U_r = 17.7$–$17.8$ (i.e. $f_s/f_o = 3$), where the $C_L$–$Y^*$ diagram is an enclosed curve (figure 11*e*,*f*), and the frequency in $C_L$ is three times that in $Y^*$ at $U_r = 17.7$–$17.8$. It can be deemed '1:3 lock-in' where $f_s$ locks in with $3f_o$. Figure 12 shows power spectra ($E_Y$ and $E_{CL}$) and envelopes of $Y^*$ and $C_L$ at $U_r = 17.5$ and 19. For $U_r = 17.5$, $f_s/f_o = 2.951 < 3$, whereas for $U_r = 19$, $f_s/f_o = 3.185 > 3$. In the power spectra of $E_Y$ (figure 12*a*,*e*), there is a minor peak ($f'_o$) on the left-hand side of $f_o$ for $U_r = 17.5$ (figure 12*a*) and on the right-hand side of $f_o$ for $U_r = 19$ (figure 12*e*). The beat frequency (i.e. the frequency of the envelope) in $Y^*$ can be represented as $f_{bY} = 1/T_{bY} = |f_o - f'_o|$ (figure 12*c*,*g*). The question is, what is the origin of $f'_o$? Generally, such a beat frequency is generated from the interference between two frequencies. One can expect this beat frequency is due to the difference between the vortex shedding frequency and cylinder vibration frequency as these two frequencies are predominantly active during the cylinder vibrations. This is, however, not the case here as is shown below.

Similarly, there is a minor peak ($f'_s$) on the right-hand side of $f_s$ (i.e. $f_s/f_o < 3$) and on the left-hand side of $f_s$ (i.e. $f_s/f_o > 3$) for $U_r = 17.5$ and 19, respectively (figure 12*b*,*f*). The corresponding beat frequency is $f_{bL} = 1/T_{bL} = |f_s - f'_s|$ (figure 12*d*,*h*).

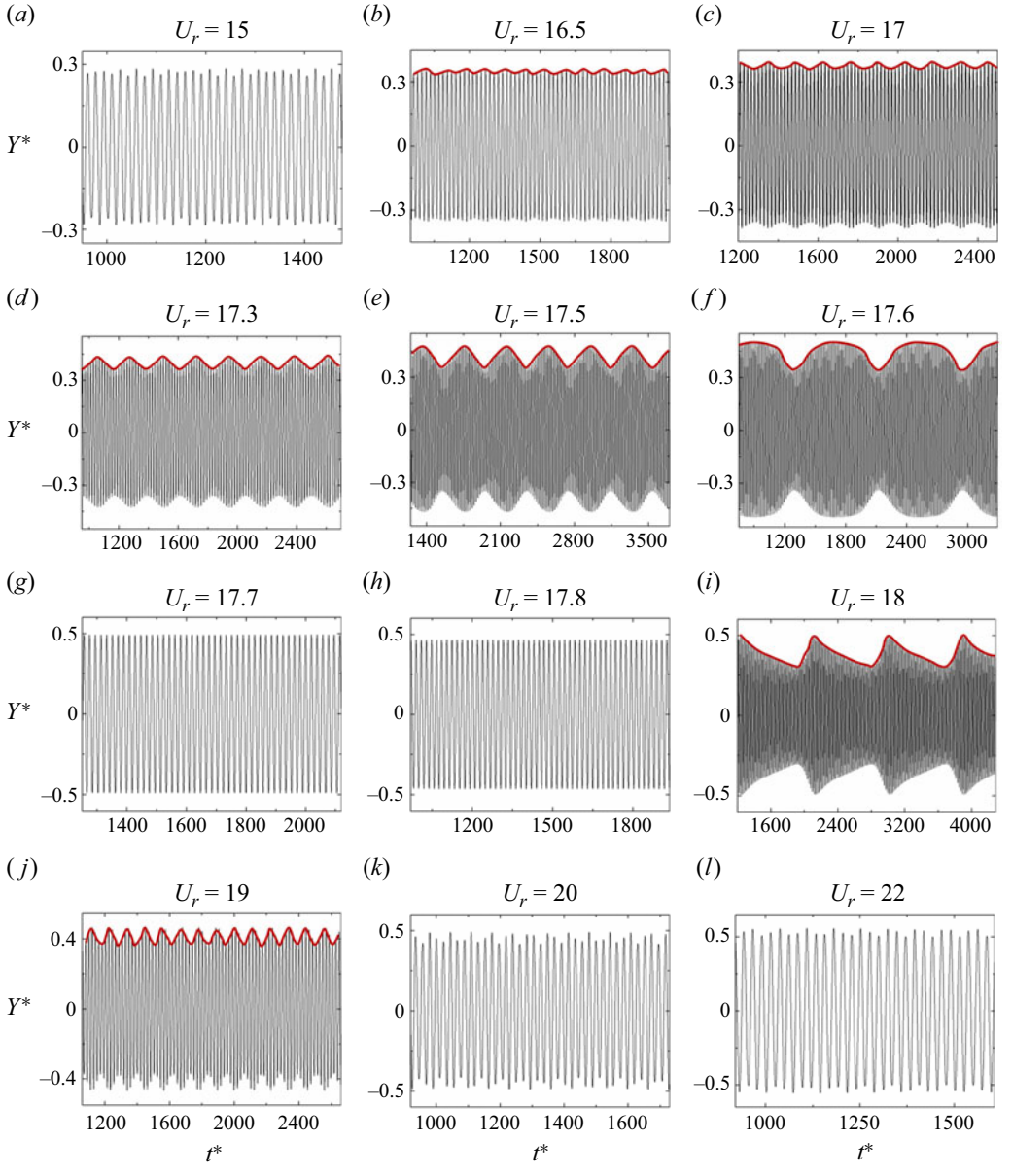


Figure 9. (*a–l*) Time histories of cylinder displacement $Y^*$ for different $U_r$. The red curve is the envelope of $Y^*$. Here, $m^* = 20$, $\zeta = 0$ and $Re = 170$.

For a given $U_r$,

$$f_{bY} = f_{bL} \quad \text{(i.e. } T_{by} = T_{bL}\text{)} \tag{3.14}$$

and

$$|f_o - f_o'| = |f_s - f_s'|. \tag{3.15}$$

It is found that $f_s' = 3f_o$.

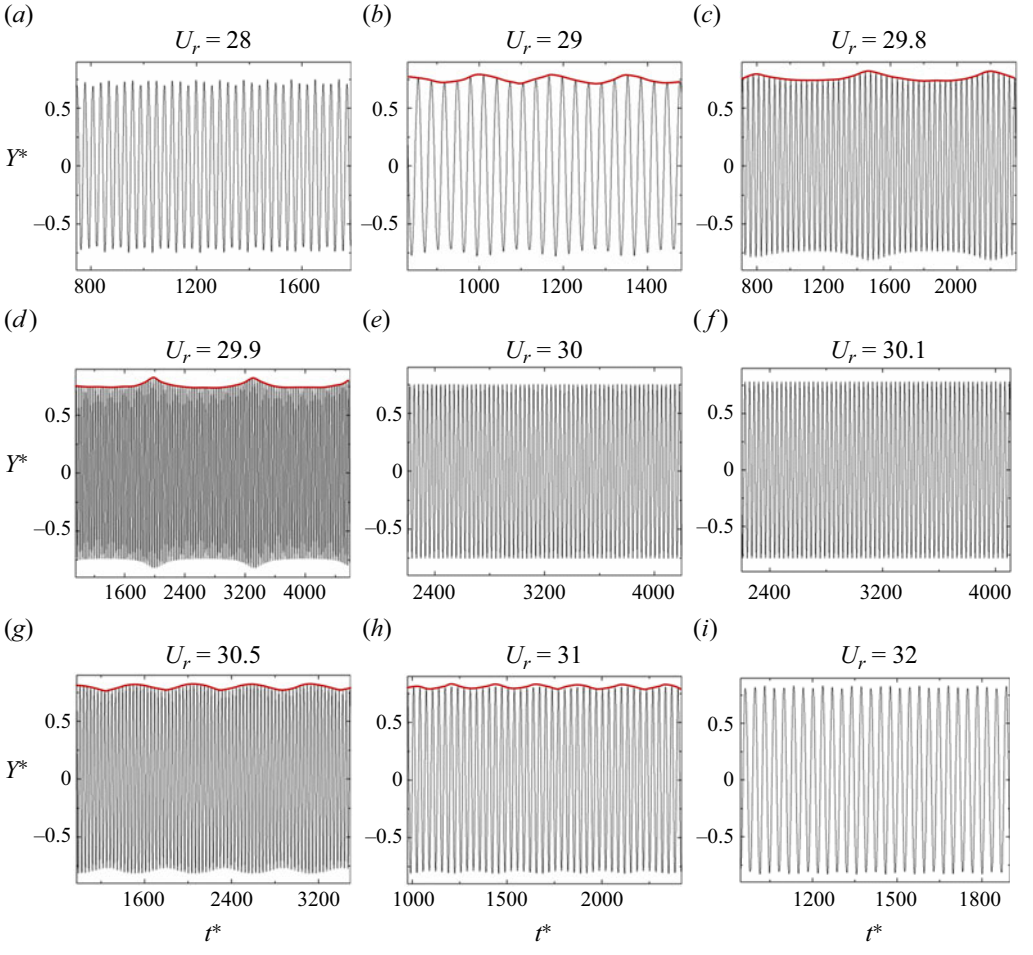


Figure 10. (*a–i*) Time histories of cylinder displacement response $Y^*$ for different $U_r$ values. Here, $m^* = 20$, $\zeta = 0$ and $Re = 170$.

Using (3.14), it can, therefore, be written as

$$|f_s - f_s'| = |f_s - 3f_o| = |f_o - f_o'|. \tag{3.16}$$

This is to say that the beat frequency in both $Y^*$ and $C_L$ is $f_b = |f_s - 3f_o|$. This explains that the beat frequency will be smaller as $f_s/f_o$ gets closer to 3, and it will be zero (no beating) when $f_s/f_o = 3$. That is, the beating phenomenon is linked to the difference between $f_s$ and $3f_o$, tending to 1:3 synchronization, not directly linked to the difference between $f_s$ and $f_o$. In GB, since $f_s/f_o$ is proportional to $U_r$ (figure 4*b*; (3.1)), the beating $U_r$ around $f_s/f_o = 3$ can be predicted from (3.1) for different values of $m^*$. The other peaks $E_{CL}$ and $E_Y$ emerge at $2f_s - f_s'$ and $2f_o - f_o'$, respectively. A beating phenomenon was also observed in some studies of the FIV of a circular cylinder associated with a mode change or mode competition. Voorhees *et al.* (2008), Zhang *et al.* (2015) and Shen *et al.* (2018) indicated that this beating is due to the difference between the vibration frequency and the vortex shedding frequency (i.e. $f_o$ and $f_s$), while Pan, Cui & Miao (2007) and Mittal (2017) claimed that the beating is the modulation between the natural frequency $f_n$ of the cylinder and the Strouhal frequency $f_{s,\,fixed}$ of the fixed cylinder. The beating phenomenon

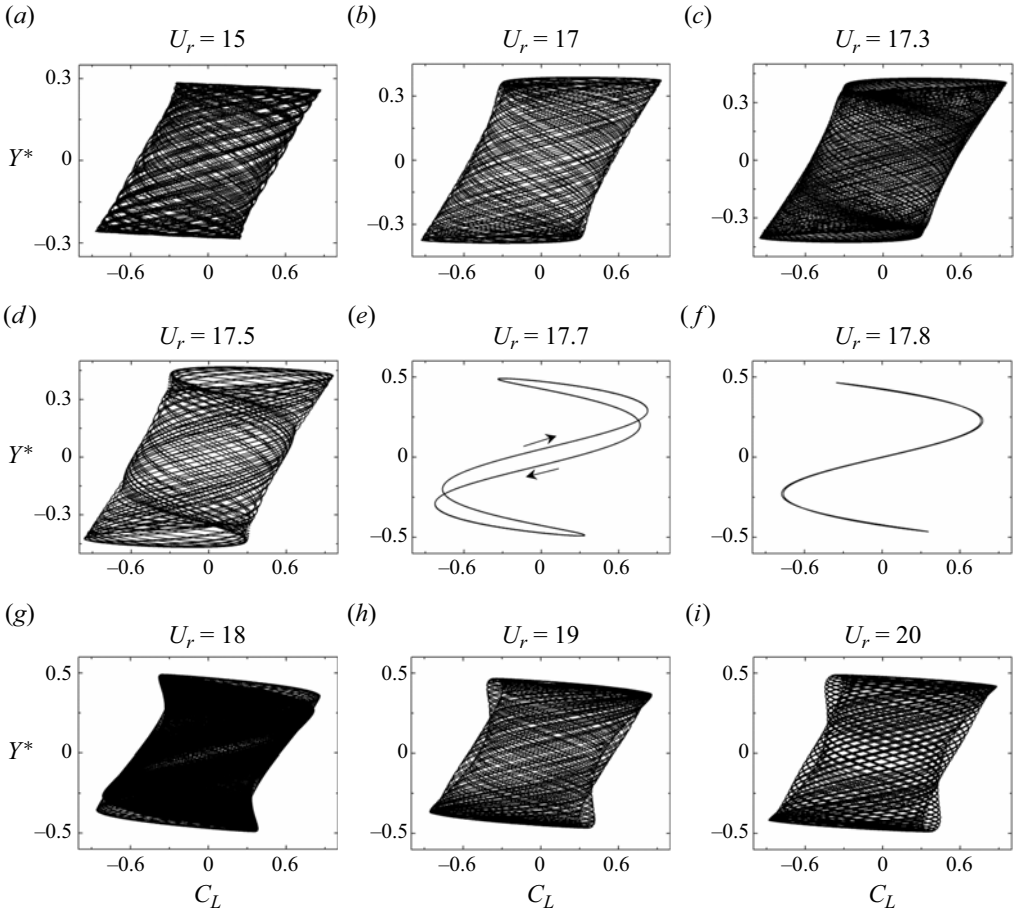


Figure 11. (*a–i*) Lissajous $C_L$–$Y^*$ diagrams for different $U_r$. Here, $m^* = 20$, $\zeta = 0$ and $Re = 170$.

of a vibrating square cylinder in GB, however, is not the same as the cases of the circular cylinder mentioned above. It is the difference between $f_s$ and $3f_o$ that gives rise to the beating phenomenon as $f_s/f_o$ gets close to 3. This observation is made for the first time.

Apart from the 1:3 synchronization mentioned above, we also observed the 1:5 synchronization ($f_s/f_o = 5$) between the vibration frequency and the shedding frequency at $U_r = 23.65$, 27.6 and 30 for $m^* = 5$, 10 and 20, respectively. Here the beat frequency $f_b = |f_s - 5f_o|$ as $f_s/f_o$ gets close to 5. The beat amplitude (figure 10) is, however, much smaller than that in the case involving 1:3 synchronization (figure 9).

### 3.6. *Effects of $m^*$, $\zeta$, $m^*\zeta$, $(m^* + m^*_{a0})\zeta$ and $(m^* + m^*_{ae})\zeta$ on $U_{rc}$ for galloping onset*

Next, we analyse the effects of $m^*$ and $\zeta$ on $U_{rc}$ for the onset of galloping. To save time and computational resources, we simulated the responses at high $U_r$ values only (figures 13 and 14). Parameter $U_{rc}$ is identified from the abrupt increase in $A^*$ (figure 13) and/or from the sudden decrease in $f_r$ (figure 14). For all $\zeta$ values examined, $A^*$ decreases with increasing $m^*$ before the galloping onset (i.e. for $U_r < U_{rc}$), which implies that $A^*$ in LB and/or DB (desynchronization branch) weakens with increasing $m^*$. However, for a given $m^*$, $A^*$ for $U_r < U_{rc}$ does not change appreciably with increasing $\zeta$. Figure 14 displays that $f_r > 1.0$

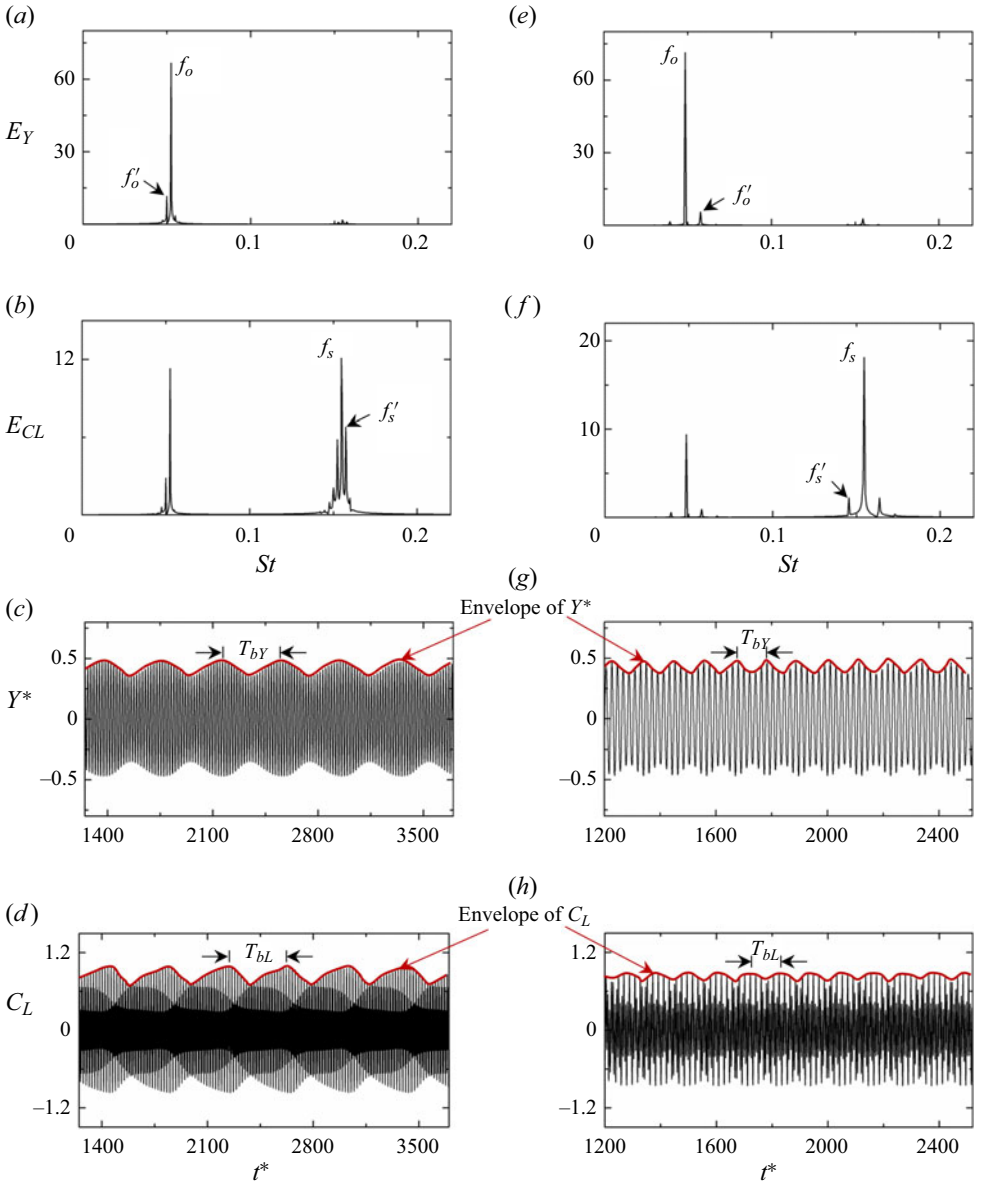


Figure 12. Power spectrum of (*a*,*e*) $Y^*$ and (*b*,*f*) $C_L$. Envelopes of (*c*,*g*) $Y^*$ and (*d*,*h*) $C_L$. (*a–d*) $U_r = 17.5$, (*e–h*) $U_r = 19$. Here, $m^* = 20$, $\zeta = 0$ and $Re = 170$.

for $U_r < U_{rc}$ but $f_r < 1.0$ for $U_r > U_{rc}$. In the latter $U_r$ regime, when $m^*$ is increased, $f_r$ increases to approach 1.0.

To further investigate the influence of $m^*$ and $\zeta$ on $U_{rc}$, more cases of $m^*$ and $\zeta$ are also considered. Table 3 summarizes $U_{rc}$ for $m^* = 2$, 3, 5, 10, 20, 30, 40 and 50 and $\zeta = 0$, 0.001, 0.01, 0.05, 0.1, 0.2, 0.4, 0.6 and 1.0 at $U_r \leq 80$. When $\zeta = 0$, $U_{rc}$ is 17, 13, 12, 12, 12, 12 and 12 for $m^* = 3$, 5, 10, 20, 30, 40 and 50, respectively, i.e. $U_{rc}$ decreases with increasing $m^*$ for $3 \leq m^* < 10$ before being insensitive to $m^*$ for $m^* \geq 10$. Figure 15 shows the dependence of galloping occurrence on $m^* = 2$–50 and $\zeta = 0$–1. No galloping is

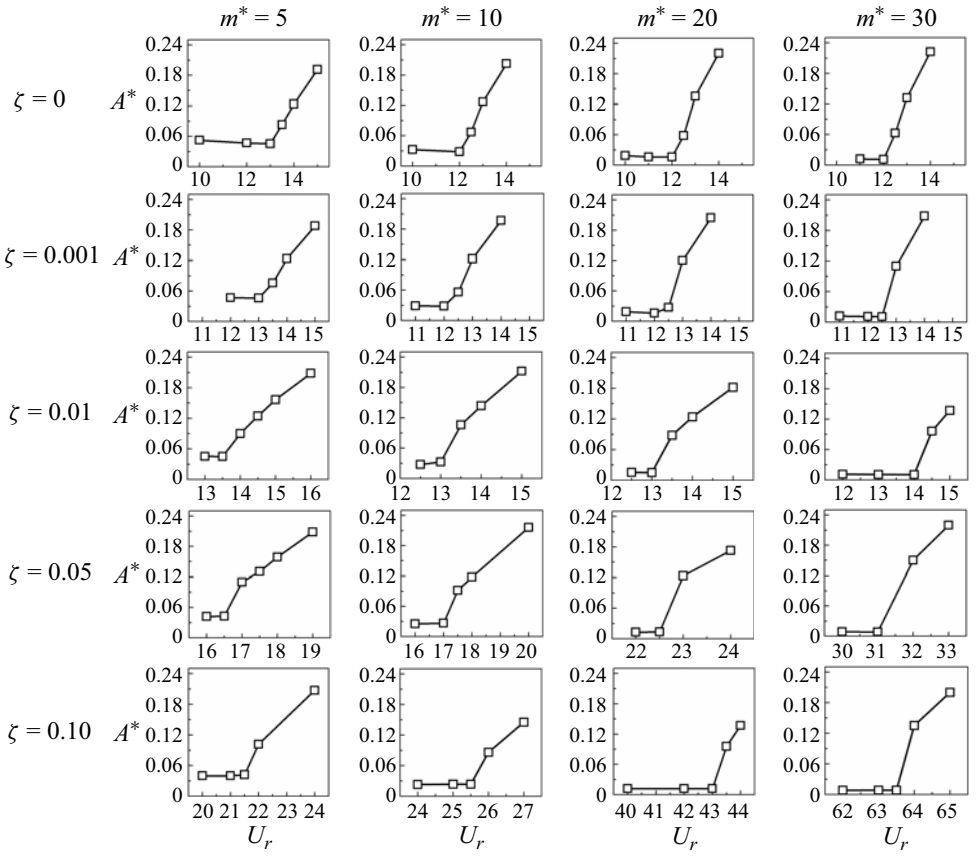


Figure 13. Variations of vibration amplitude $A^*$ with reduced velocity $U_r$ for different $m^*$ and $\zeta$ values. Here, $Re = 170$.

observed at $m^* = 2$ for all $\zeta$ values examined. Galloping is observed for $m^* = 3$–10 when $\zeta = 0.2$, while the same occurs at $m^* = 5$ only for $\zeta = 0.4$. For $\zeta \geq 0.6$, no galloping is observed, regardless of $m^*$, until $U_r = 80$ examined. When $m^*$ is increased from 5 (i.e. $m^* \geq 5$), $U_{rc}$ changes insignificantly for $\zeta \leq 0.01$, but significantly for $\zeta \geq 0.05$ (table 3, figure 16*a*). Parameter $U_{rc}$, however, significantly increases when $m^*$ is decreased from 5 to 3 for all $\zeta$ values (table 3, figure 16*b*). For all $m^*$ values examined, an increase in $\zeta$ makes $U_{rc}$ higher, particularly when $\zeta > 0.01$ (table 3, figure 16*b*). That is, the effect of $\zeta$ on $U_{rc}$ is insignificant for $\zeta \leq 0.01$ but significant for $\zeta > 0.01$, a higher $\zeta$ suppressing the cylinder vibration. Joly *et al.* (2012) also found a higher $U_{rc}$ value at $\zeta = 0.1$ than that at $\zeta = 0$.

The three-dimensional view of the dependence of $U_{rc}$ on $m^*$ and $\zeta$ shown in figure 17 allows us to observe the variations of $U_{rc}$ with $m^*$ and $\zeta$ more intuitively at $\zeta \leq 0.2$. The value of $U_{rc}$ achieves its maximum at $m^* = 30$ and $\zeta = 0.1$. For all $m^*$ values, an increase in $\zeta$ leads to a larger $U_{rc}$. The increase is, nevertheless, larger for a large $m^*$. Particularly for $\zeta > 0.01$, $U_{rc}$ declines for $m^* \leq 5$ and rapidly increases with increasing $m^*$. The degree of the decrease and/or increase becomes larger for a higher $\zeta$ value.

Some researchers have debated whether $m^*\zeta$ can serve as the FIV criterion of a circular cylinder. Griffin, Skop & Ramberg (1975) and Griffin (1980) used a Skop–Griffin

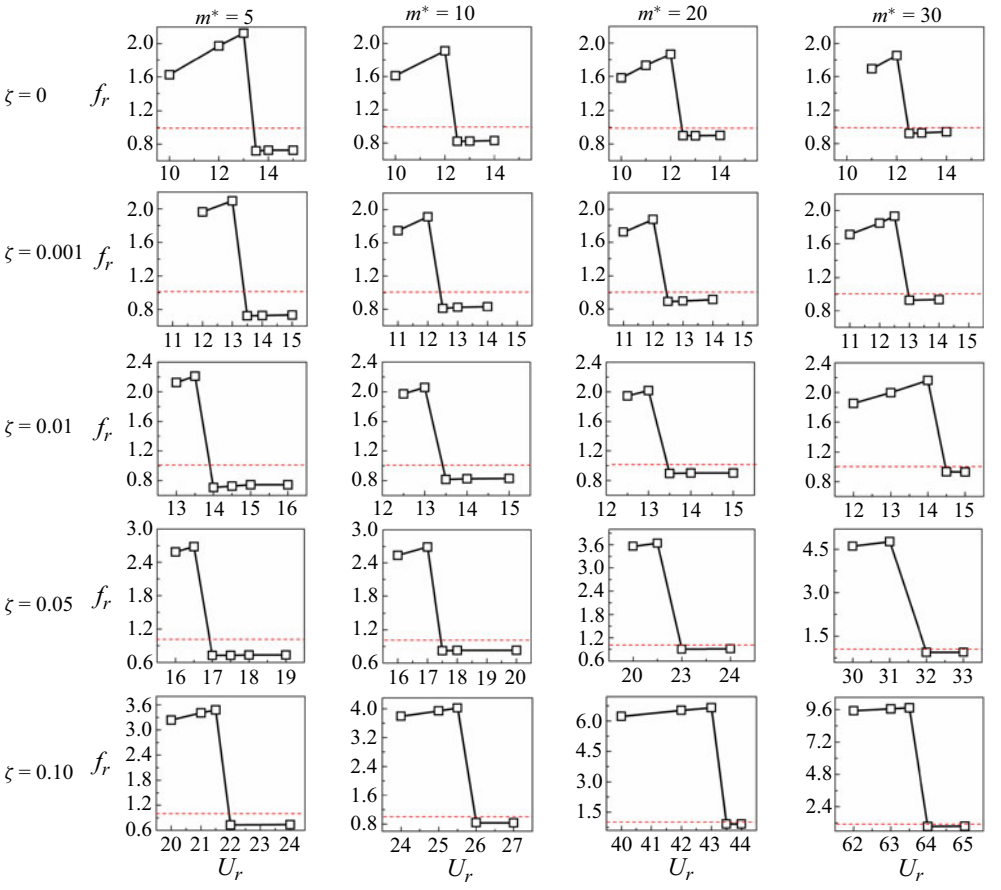


Figure 14. Variations of frequency ratio $f_r$ with reduced velocity $U_r$ for different $m^*$ and $\zeta$. The red dotted line represents $f_r = 1$. Here, $Re = 170$.

| $\zeta$ | 0 | 0.001 | 0.01 | 0.05 | 0.1 | 0.2 | 0.4 | 0.6 | 1 |
|---|---|---|---|---|---|---|---|---|---|
| $m^* \leq 2$ | — | — | — | — | — | — | — | — | — |
| $m^* = 3$ | 17 | 17 | 18 | 22 | 28 | 44 | — | — | — |
| $m^* = 5$ | 13 | 13 | 13.5 | 16.5 | 21.5 | 34 | 67.5 | — | — |
| $m^* = 10$ | 12 | 12 | 13 | 17 | 25.5 | 50 | — | — | — |
| $m^* = 20$ | 12 | 12 | 13 | 22.5 | 43 | — | — | — | — |
| $m^* = 30$ | 12 | 12.5 | 14 | 31 | 63.5 | — | — | — | — |
| $m^* = 40$ | 12 | 12.5 | 14 | 40 | — | — | — | — | — |
| $m^* = 50$ | 12 | 12.5 | 15 | 50 | — | — | — | — | — |

Table 3. Effects of $m^*$ and $\zeta$ on $U_{rc}$. '—' means no galloping observed for $U_r \leq 80$ examined.

parameter $S_G$ ($= 2\pi^3 S^2 m^* \zeta$, where $S$ is the Strouhal number of the static cylinder) to plot the maximum vibration amplitude $A^*_{max}$ against $S_G$ (i.e. $m^*\zeta$). It is known as the Griffin plot. However, this plot showed a large scatter of $A^*_{max}$ data. Later, Khalak & Williamson (1999) and Govardhan & Williamson (2000) introduced a combined parameter $(m^* + m^*_{a0})\zeta$ to modify the Griffin plot, where $m^*_{a0}$ (i.e. potential added-mass ratio $C_A$ in

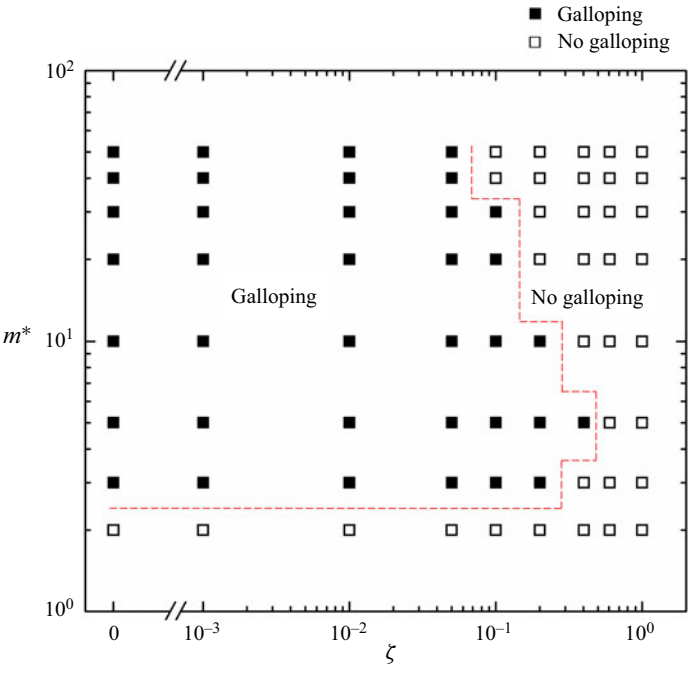


Figure 15. Dependence of galloping occurrence on $m^* = 2$–$50$ and $\zeta = 0$–$1$. Here, $Re = 170$.

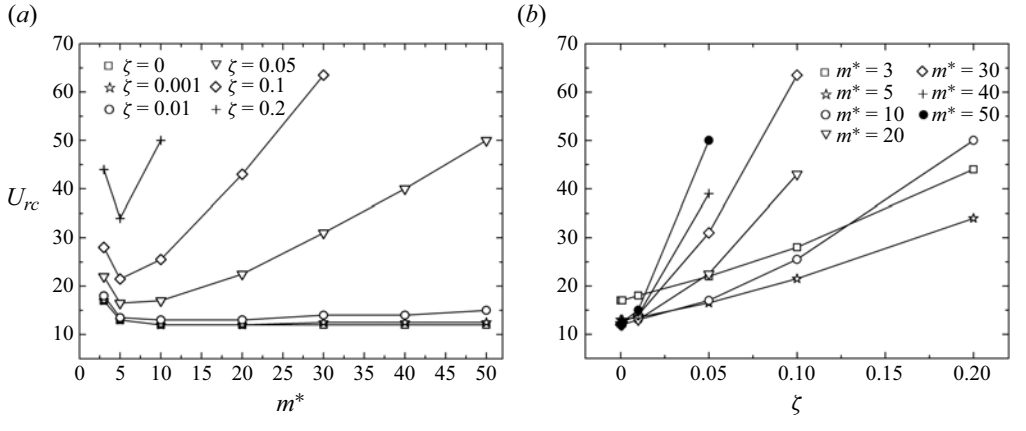


Figure 16. Effect of (*a*) mass ratio $m^*$ and (*b*) damping ratio $\zeta$ on critical reduced velocity $U_{rc}$. Here, $Re = 170$.

their investigations) is the quiescent-fluid added-mass ratio and is about 1.0 for a circular cylinder. They demonstrated that $(m^* + m^*_{a0})\zeta$ collapses the $A^*_{max}$ data well for a wide range of $(m^* + m^*_{a0})\zeta > 0.06$. Sarpkaya (1978, 1995) stated that the vibration response depends on $m^*\zeta$ for $S_G > 1$ (i.e. $m^*\zeta > 0.4$), while it depends on $m^*$ and $\zeta$ separately rather than on $m^*\zeta$ for $m^*\zeta < 0.4$. Blevins & Coughran (2009) for two-degrees-of-freedom vibration found that the ratio of inline to transverse amplitudes is governed by $m^*$ and $\zeta$ independently. Bahmani & Akbari (2010) claimed that $m^*\zeta$ can be used to characterize $A^*_{max}$ with an acceptable accuracy. For a cylinder submerged in the wake of another cylinder, Alam (2021) claimed that $m^*\zeta$ (i.e. $m^*\zeta = 0$–$8$) does not serve as a unique

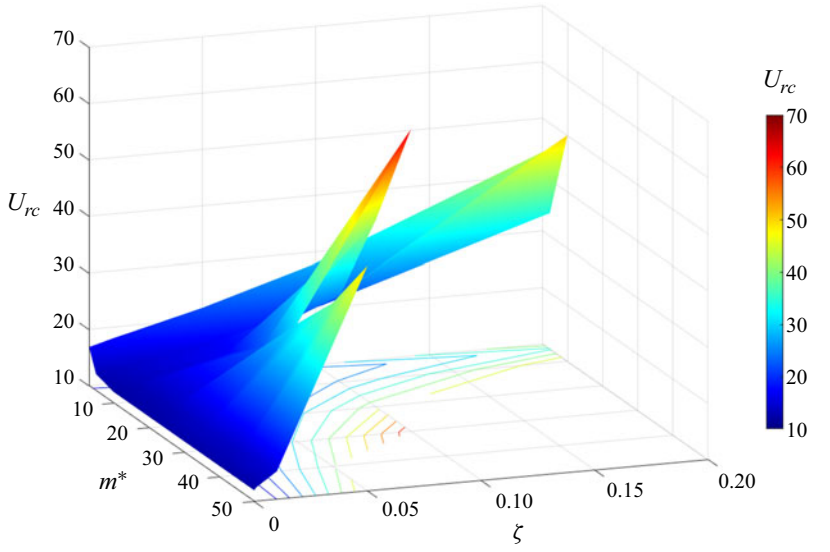


Figure 17. Relationship of $U_{rc}$ with $m^*$ (= 3–50) and $\zeta$ (= 0–0.2). Here, $Re = 170$.

parameter to characterize the vibration amplitude. In addition, Bearman (1984) reported that low values of $m^*$ affect the frequency ratio independently, not $m^*\zeta$. Williamson & Goverdhan (2004) and Govardhan & Williamson (2004) demonstrated that the VIV range depends only on $m^*$ at $(m^* + C_A)\zeta < 0.05$. Here, we will see whether $m^*\zeta$ or $(m^* + m^*_{a0})\zeta$ works well to collapse $U_{rc}$ data. If not, what is the intrinsic parameter that dictates the vibration? Figure 18(*a*,*b*) shows the relationships of $U_{rc}$ with $m^*\zeta$ and $(m^* + m^*_{a0})\zeta$. As shown in figure 18(*a*), there are more than one $U_{rc}$ data point, significantly different, for a given $m^*\zeta$ (e.g. three $U_{rc}$ values for $m^*\zeta = 1.0$ and four $U_{rc}$ values for $m^*\zeta = 2.0$), which indicates that $m^*\zeta$ cannot serve as the only criterion for galloping onset. In figure 18(*b*), the $U_{rc}$ data scattering alleviates, which points to a linear increase in $U_{rc}$ with $(m^* + m^*_{a0})\zeta$ overall at $m^* \geq 5$. But still, there are some scattered data points, and the collapse of $U_{rc}$ data on a line is still not credible. It hints that something is still missing in $(m^* + m^*_{a0})\zeta$. We find the missing parameter here.

As $m^*$ decreases, $f_r$ in GB deviates considerably from unity, i.e. the vibration frequency differs from the natural frequency (figures 5*b* and 14). The deviation is attributed to the flow-induced added mass $m^*_{af}$ that should be considered in $(m^* + m^*_{a0})\zeta$. The effective added mass is the quiescent-fluid added mass plus flow-induced added mass, i.e. $m^*_{ae} = m^*_{a0} + m^*_{af}$ (Alam 2022). While $m^*_{a0}$ is independent of $U_r$, $m^*_{af}$ is highly dependent on $U_r$ and markedly changes at $U_{rc}$. Therefore, $m^*_{af}$ is crucial and should be added with $m^*_{a0}$. That is, in the mass-damping parameter, we have to consider $m^*_{ae}$, not $m^*_{a0}$, i.e. $(m^* + m^*_{a0})\zeta$ should be replaced by $(m^* + m^*_{ae})\zeta$. As shown in figure 7(*f*), $m^*_{ae}$ jumps at $U_{rc}$ and declines with increasing $m^*$ and $U_r$. We consider $m^*_{ae}$ at the galloping onset for $(m^* + m^*_{ae})\zeta$, and the dependence of $U_{rc}$ on $(m^* + m^*_{ae})\zeta$ is presented in figure 19. For $(m^* + m^*_{ae})\zeta > 0.55$, as shown in figure 19(*a*), the $U_{rc}$ data points collapse well on a line at $m^* \geq 5$, showing that $U_{rc}$ linearly increases with $(m^* + m^*_{ae})\zeta$. The relationship between $U_{rc}$ and $(m^* + m^*_{ae})\zeta$ can be represented by a curve-fitting equation:

$$U_{rc} = 17.4(m^* + m^*_{ae})\zeta + 2.5 \quad (\text{for } (m^* + m^*_{ae})\zeta > 0.55 \text{ and } m^* \geq 5). \tag{3.17}$$

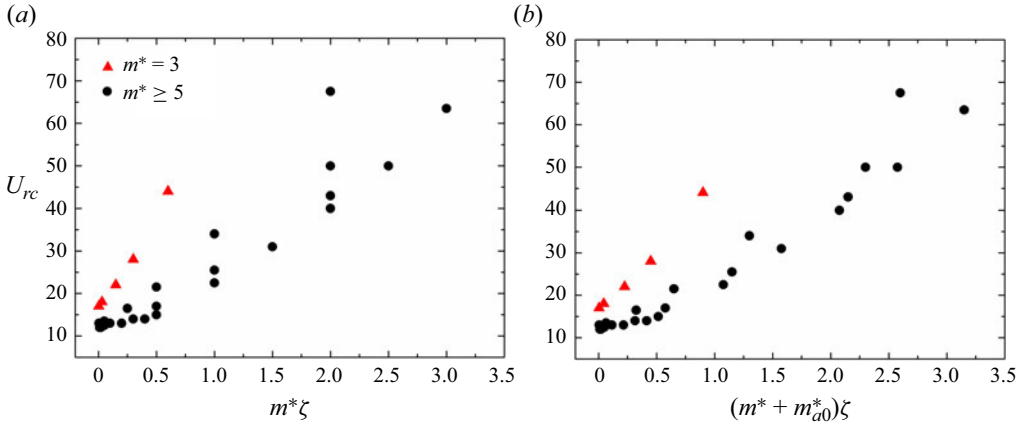


Figure 18. Combined mass-damping parameter (*a*) $m^*\zeta$ and (*b*) $(m^* + m^*_{a0})\zeta$ with critical reduced velocity $U_{rc}$. Here, $Re = 170$.

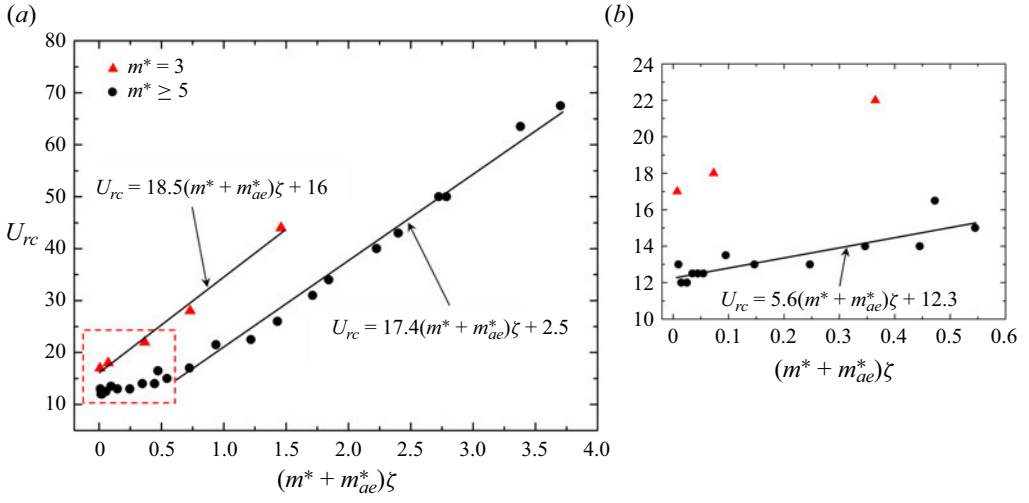


Figure 19. (*a*) Relationship between critical reduced velocity $U_{rc}$ and combined mass-damping parameter $(m^* + m^*_{ae})\zeta$. (*b*) Zoomed-in view of $U_{rc}$ variations at $(m^* + m^*_{ae})\zeta \leq 0.55$.

For $(m^* + m^*_{ae})\zeta \leq 0.55$ as shown in figure 19(*b*), the $U_{rc}$ also increases linearly, albeit with a smaller slope, with increasing $(m^* + m^*_{ae})\zeta$ for $m^* \geq 5$. The $U_{rc}$ data points for $m^* = 5$ appear more scattered when $(m^* + m^*_{ae})\zeta > 0.55$. The linear relationship at $(m^* + m^*_{ae})\zeta \leq 0.55$ and $m^* \geq 5$ can be represented as

$$U_{rc} = 5.6(m^* + m^*_{ae})\zeta + 12.3 \quad (\text{for } (m^* + m^*_{ae})\zeta \leq 0.55 \text{ and } m^* \geq 5). \tag{3.18}$$

Equation (3.18) further proves that when $\zeta = 0$ or is very small, $U_{rc}$ becomes independent ($U_{rc} = 12.3$) of $m^*$, which is consistent with the observation made in figure 16(*a*).

For $m^* = 3$, $U_{rc}$ again linearly increases with $(m^* + m^*_{ae})\zeta$, with a larger slope than the case for $m^* \geq 5$ (figure 19*a*). The relationship between $U_{rc}$ and $(m^* + m^*_{ae})\zeta$ can be expressed as

$$U_{rc} = 18.5(m^* + m^*_{ae})\zeta + 16 \quad (\text{for } m^* = 3). \tag{3.19}$$

The slopes of $U_{rc}$ in (3.17) and (3.19) are close to each other although the $U_{rc}$ intercepts differ between the two cases.

The use of $(m^* + m^*_{ae})\zeta$ in (3.17)–(3.19) can predict $U_{rc}$. Term $(m^* + m^*_{ae})\zeta$ can, therefore, be considered a criterion for the prediction of galloping onset. Equation (3.17) also illustrates why galloping is not observed for $m^* = 20$ and $\zeta = 0.2$, where $(m^* + m^*_{ae})\zeta = 4.76$. The value of $U_{rc}$ predicted by (3.17) is $85.19 > 80$ examined. It can therefore be concluded that the criterion for a fluid–structure system is $(m^* + m^*_{ae})\zeta$, not $m^*\zeta$ or $(m^* + C_A)\zeta$ or $(m^* + m^*_{a0})\zeta$. For a given $(m^* + m^*_{ae})\zeta$, $U_{rc}$ is higher for $m^* < 5$ than for $m^* \geq 5$. There is a threshold of $m^*$ $(= 5)$ after $(m^* \geq 5)$ or before $(m^* < 5)$ which the relationships between $U_{rc}$ and $(m^* + m^*_{ae})\zeta$ differ. We further shed light on this threshold in the next section.

### 3.7. *Underlying physics of $m^*$ and $\zeta$ effects on galloping onset*

#### 3.7.1. *Effects of $m^*$ and $\zeta$ when $\zeta = 0$*

Using the global linear stability analysis method, Meliga & Chomaz (2011), Zhang *et al*. (2015) and Yao & Jaiman (2017) investigated the mechanism of VIVs of a freely vibrating cylinder. They identified two modes responsible for the onset of instability in the fluid–structure system: wake mode (WM) and structure mode (SM). These two leading modes have a strong coupling for low $m^*$, while they are decoupled for high $m^*$. Parameter $m^*$ plays an important role in the selection of the leading mode. The essential characteristic of the flutter-induced lock-in is the competition between the two unstable modes (Zhang *et al*. 2015). Li *et al*. (2019) utilized linear stability analysis and direct numerical simulations to investigate the underlying mechanisms of galloping of a square cylinder with zero damping. They concluded that the unstable SM leads to the low-frequency large-amplitude vibration of the cylinder, while the unstable WM results in the high-frequency vortex shedding in the wake. The instability of SM is the primary cause of the galloping phenomenon. The onset of galloping is postponed when SM and WM compete with each other. As such, the galloping phenomenon can be completely suppressed or $U_{rc}$ can be delayed at relatively low-$Re$ and low-$m^*$ $(< 5)$ conditions. In their study, the galloping vibration completely disappeared for low $m^*$ $(m^* < 4,\ Re = 150)$ because of the strong competition between the enhanced SM and WM at low $m^*$ (lighter structure). They also introduced a 'pre-galloping' region, located between VIV and galloping, where galloping does not occur but the SM is unstable.

Here, we investigate the influence of $m^*$ on galloping by analysing the high-frequency $(f_s)$ and low-frequency $(f_o)$ signals of the vibration. At $\zeta = 0$, $U_{rc}$ remains constant for $m^* \geq 10$ while it increases with decreasing $m^*$ for $3 \leq m^* < 10$. Ultimately, galloping is suppressed for $m^* \leq 2$, i.e. a relatively low $m^*$ inhibits galloping. Given that the maximum $U_r$ examined in this study is 80, galloping may be observed for a smaller $m^*$ $(\leq 2)$ if $U_r$ is further increased (Han & Langre 2022). It has already been shown that the high-pass-filtered $C_L$ and $Y^*$ associated with the vortex shedding are antiphase, not auspicious for the cylinder vibration. Conversely, the low-pass-filtered signals are in phase, auspicious for the cylinder vibration. First, we analyse vibration signals $(Y^*)$ at $m^* = 20$ with $U_r = 12$ and 13, corresponding to pre-galloping and galloping regions, respectively (figure 20*a*,*d*). To gain insight into the evolution of the frequency content over time, the continuous wavelet transform (CWT) is performed using the Morlet wavelet (figure 20*b*,*e*). The wavelet centre frequency $Fc = 3$ and the wavelet scales equal $2Fc$–$2Fc \times 2^{14}$, which allows us to measure frequency in the range of $Fs/2^{14}$–$Fs/2$ (where $Fs$ is the sampling frequency). Additionally, power spectra of vibration responses in different developing

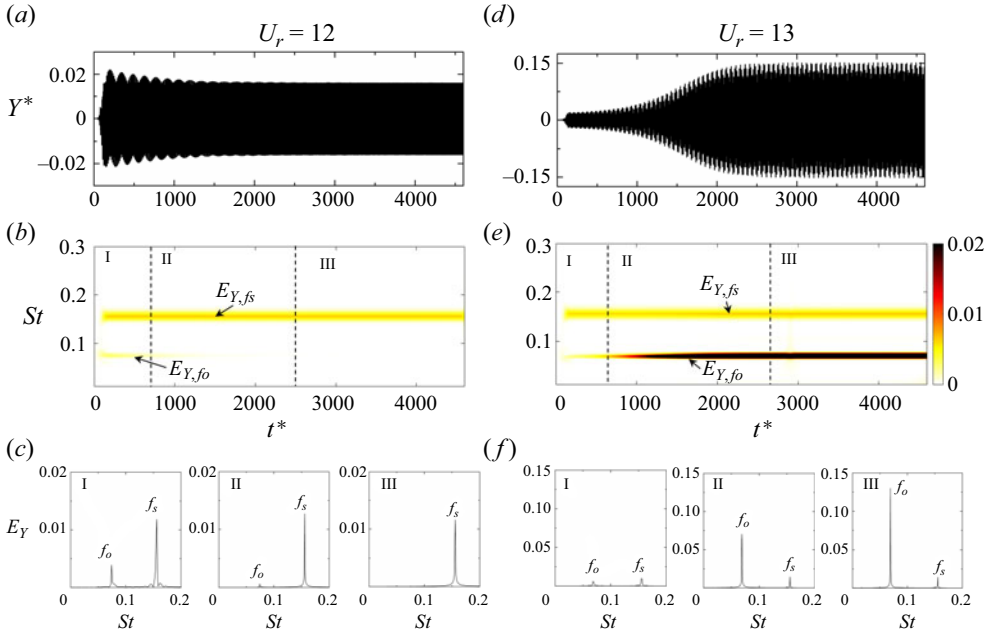


Figure 20. (*a*,*d*) Time histories of $Y^*$. (*b*,*e*) Time–frequency spectrum of $Y^*$ based on CWT. (*c*,*f*) Power spectral density functions of $Y^*$ at different regimes. (*a*–*c*) $m^* = 20$, $U_r = 12$; and (*d*–*f*) $m^* = 20$, $U_r = 13$. Here, $\zeta = 0$ and $Re = 170$.

regimes are shown in figure 20(*c*,*f*). The cylinder vibration in each signal comprises two distinct frequencies $f_o$ and $f_s$, associated with SM and WM, respectively. Consider $E_{Y,fo}$ and $E_{Y,fs}$ as the energy intensity at $f_o$ and $f_s$, respectively.

In the pre-galloping region, the vibration amplitude rapidly develops and reaches its maximum at $t^* \approx 200$ (figure 20*a*). At $t^* < 800$, there is an intensified competition between $f_o$ and $f_s$, where $E_{Y,fo}$ and $E_{Y,fs}$ are considerable (figure 20*c*); this transition is marked as regime I. In regime II, $E_{Y,fo}$ rapidly decreases and becomes insignificant while $E_{Y,fs}$ dominates the competition, suppressing the vibration at $f_o$ (figure 20*c*). In regime III ($t^* > 2500$), the cylinder vibration solely occurs at $f_s$, and the amplitude remains constant.

After galloping, $E_{Y,fo}$ increases gradually in regimes I and II, and it remains unchanged in regime III (figure 20*e*). In regime I, $E_{Y,fo}$ is lower than $E_{Y,fs}$ (figure 20*f*). Parameter $E_{Y,fo}$ increases and $E_{Y,fs}$ remains unchanged from regimes I to II; eventually, $E_{Y,fo}$ becomes larger than $E_{Y,fs}$. This indicates that SM dominates the competition and results in the occurrence of galloping. In regime III, $E_{Y,fo}$ remains unchanged, with $E_{Y,fo}/E_{Y,fs} = 7.92$ (figure 20*f*).

The $E_Y$ values can be used to characterize the vibration amplitude. As shown in figure 21, the cylinder vibration is decomposed into low-frequency and high-frequency vibrations after the commencement of galloping. We define the vibration amplitudes of the low- and high-pass-filtered $Y^*$ as $A^*_{low}$ and $A^*_{high}$ corresponding to $E_{Y,fo}$ and $E_{Y,fs}$, respectively. In the pre-galloping region, the vibration amplitude $A^*$ in regime III can also be characterized by $E_{Y,fs}$, which declines gently with increasing $U_r$ (figures 4*a* and 21). After the onset of galloping, $A^*_{high}$ remains almost unchanged. The almost unchanged $E_{Y,fs}$ and $A^*_{high}$ nearly before the galloping occurrence and after the galloping occurrence indicate that vortex shedding is not involved in the occurrence of galloping. The value of

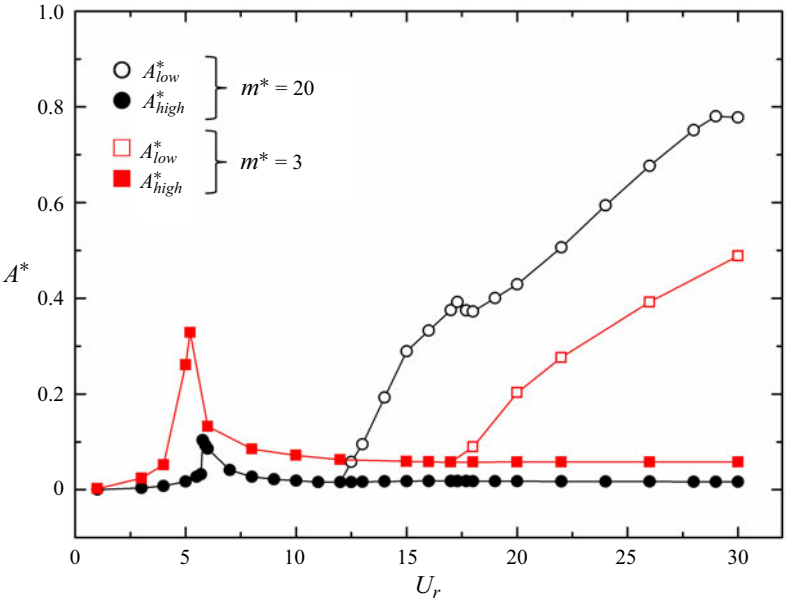


Figure 21. Dependence of $A^*$ on $U_r$ and $m^*$. Here, $\zeta = 0$ and $Re = 170$.

$A^*_{low}$, however, increases markedly with the increase of $U_r$ in the galloping regime. It is the low-frequency motion (SM) that is auspicious for the cylinder vibration, and consequently promotes the occurrence of galloping. As shown in figure 20(*b*,*e*), $E_{Y,fo}$ at $m^* = 20$ and 13 is significantly greater than that at $U_r = 12$, while $E_{Y,fs}$ is almost the same.

Since $U_{rc}$ is delayed with a decrease in $m^*$ from 5 to 3 and galloping is suppressed for $m^* = 2$ (table 3, figure 16*a*), we will further investigate the mode competition phenomenon at $m^* = 3$ to evaluate to influence of $m^*$ on the competition. At $m^* = 3$, both $A^*$ in pre-galloping region and $A^*_{high}$ in galloping regime increase compared to that at $m^* = 20$ (figure 21), and the $E_{Y,fs}$ value at $m^* = 3$ is significantly intensified (figures 20*b*,*e* and 22*b*,*e*). Consequently, the competition between $E_{Y,fo}$ and $E_{Y,fs}$ becomes more intense at $m^* = 3$, with $E_{Y,fo}/E_{Y,fs} = 1.52$ at the galloping onset in regime III (figure 22*f*). It can be inferred that if $m^*$ is further decreased, $E_{Y,fs}$ could completely overpower $E_{Y,fo}$ and suppress galloping. At the galloping onset, $E_{Y,fo}/E_{Y,fs}$, i.e. $A^*_{low}/A^*_{high}$, diminishes with decreasing $m^*$. It can be reasonably inferred that if $A^*_{low}/A^*_{high}$ at the galloping onset drops to 1 with a further decrease in $m^*$, then galloping will be completely suppressed. Figure 23 presents the influence of $A^*_{low}/A^*_{high}$ on $m^*$ at the galloping onset. It can be seen that $A^*_{low}/A^*_{high}$ decreases linearly with decreasing $m^*$, and can be represented by a curve-fitting equation:

$$A^*_{low}/A^*_{high} = 0.41m^* + 0.155. \tag{3.20}$$

When $A^*_{low}/A^*_{high} = 1$, the critical $m^*$ predicted by (3.20) is $m^*_c = 2.06 \approx 2$. Equation (3.20) explains why galloping is not observed for $m^* \leq 2$. Additionally, we observed galloping at $m^* = 2.5$ and $U_r = 40$, further verifying the rationality of the prediction of $m^*_c$. Figure 23 also shows the dependence of $A^*_{low}/A^*_{high}$ on $m^*$ at $Re = 150$ and 160, where $A^*_{low}/A^*_{high}$ declines with decreasing $m^*$, the declining rate increasing with decreasing $Re$. When $A^*_{low}/A^*_{high}$ decreases to 1, $m^*_c$ is larger at a smaller $Re$.

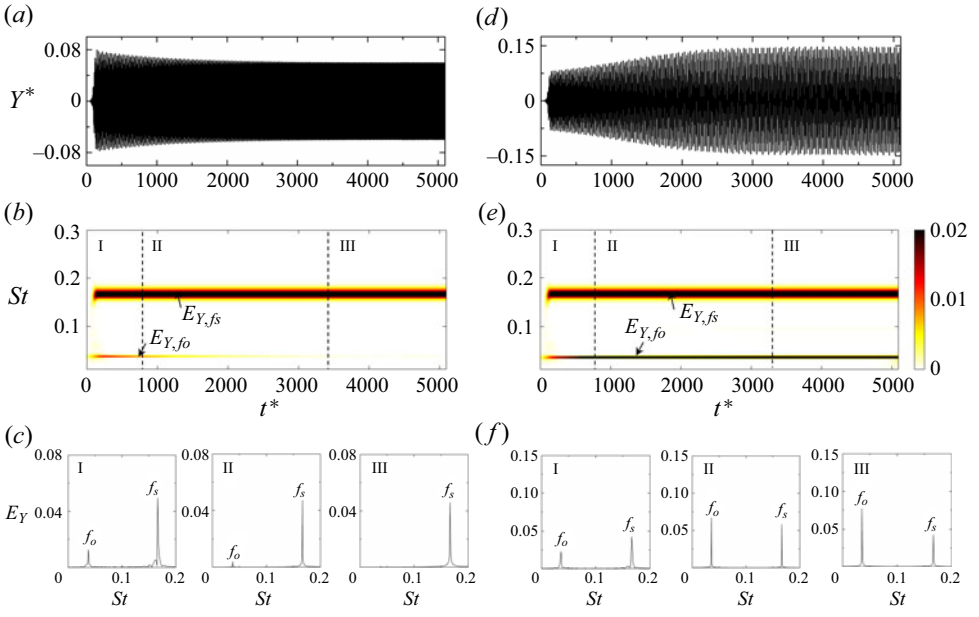


Figure 22. (*a*,*d*) Time histories of $Y^*$. (*b*,*e*) Time–frequency spectrum of $Y^*$ based on CWT. (*c*,*f*) Power spectral density functions of $Y^*$ at different regimes. (*a–c*) $m^* = 3$, $U_r = 17$; and (*d–f*) $m^* = 3$, $U_r = 18$. Here, $\zeta = 0$ and $Re = 170$.

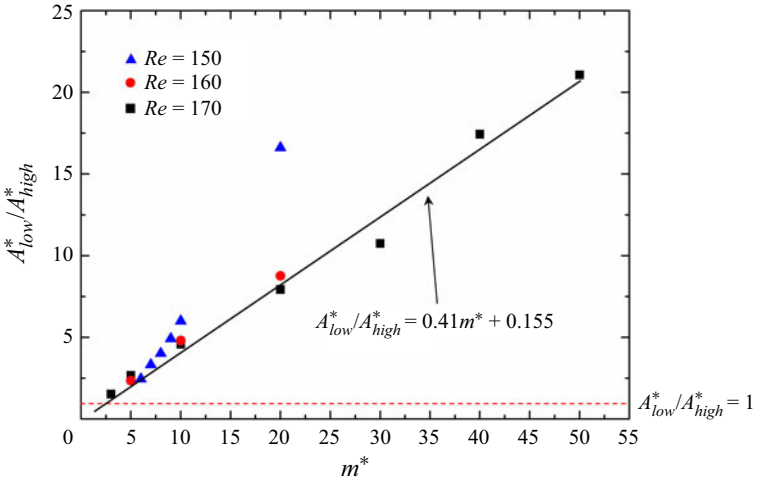


Figure 23. Effect of $m^*$ and $Re$ on $A^*_{low}/A^*_{high}$ at the galloping onset. Here, $\zeta = 0$.

In summary, at $\zeta = 0$, as $m^*$ decreases, the contribution of WM becomes more significant, leading to a delay in the onset of galloping. Eventually, galloping can be completely suppressed at sufficiently low $m^*$ values. At $m^* = 3$, the occurrence of galloping at $\zeta = 0$ depends on the competition between SM and WM while the competition is contingent on $m^*$. However, at $m^* \geq 5$, the contribution of WM becomes negligible; the cylinder vibration is thus dominated by SM, leading to a constant $U_{rc}$ as $m^*$ increases.

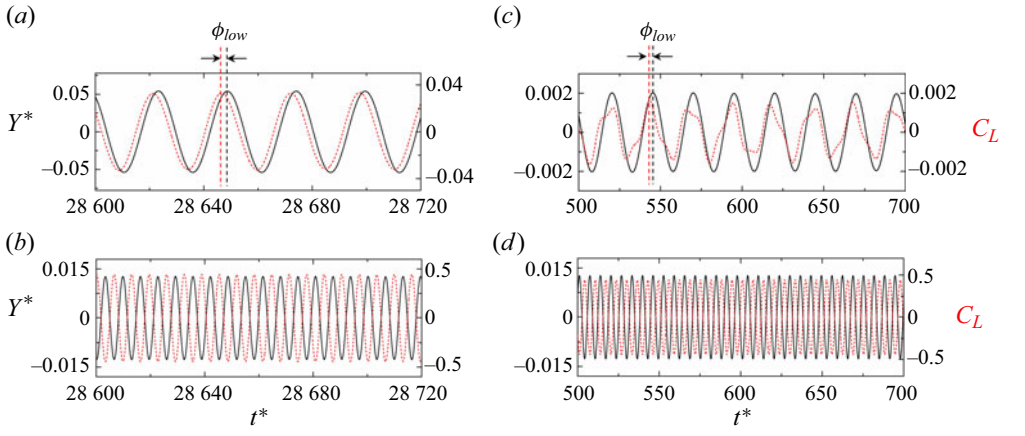


Figure 24. Time histories of (*a*,*c*) low-pass-filtered and (*b*,*d*) high-pass-filtered $Y^*$ (black lines) and $C_L$ (red lines) in GB. (*a*,*b*) $m^* = 20$, $\zeta = 0.05$ and $U_r = 23$ in regime III; (*c*,*d*) $m^* = 20$, $\zeta = 0.05$ and $U_r = 22.5$ in regime I. Here, $Re = 170$.

### 3.7.2. *Effects of $m^*$ and $\zeta$ when $\zeta > 0$*

Moving on to discussing the influence of $\zeta$ on galloping, we observe that at $\zeta > 0$, $U_{rc}$ increases with the increase of $\zeta$. Additionally, $U_{rc}$ shows a nonlinear relationship with $m^*$, initially decreasing and then increasing as $m^*$ increases. When $\zeta = 0$ or is small, $U_{rc}$ is independent of $m^*$ ($\geq 5$). As previously discussed with figure 7, when the cylinder vibrates in GB without damping ($\zeta = 0$), the phase lag between the low-pass-filtered $C_L$ and $Y^*$ is 0° (figure 7*c*), while that between the high-pass-filtered $C_L$ and $Y^*$ is 180° (figure 7*d*). As $\zeta$ increases from 0, taking $\zeta = 0.05$ and $m^* = 20$ as an example, where $U_{rc} = 22.5$, the phase lag $\phi_{low}$ (in degrees) between the low-pass-filtered $C_L$ and $Y^*$ at $U_r = 23$ (beyond the galloping onset) undergoes a shift from 0 to a positive value, i.e. $\phi_{low} \approx 27°$ (figure 24*a*). As discussed with figure 20(*a–c*), in regime I of the pre-galloping region, the cylinder vibration consists of both high- and low-frequency components. Therefore, at $\zeta = 0.05$, $\phi_{low} \approx 26.5°$ is achieved in regime I of the pre-galloping region (i.e. $U_r = 22.5$) (figure 24*c*). The phase lag between the high-pass-filtered $C_L$ and $Y^*$ at $\zeta > 0$, however, remains 180° both before and after $U_{rc}$ (figure 24*b*,*d*). Therefore, the presence of damping ($\zeta > 0$) introduces a positive phase lag between the low-pass-filtered $C_L$ and $Y^*$, both before and after galloping, modifying the coupling between the flow and cylinder vibration.

Figure 25(*a*) demonstrates the variations of $m^*_{ae}$, $\zeta_a$ and $\phi_{low}$ with $U_r$ at $m^* = 20$, $\zeta = 0.05$. In GB, $m^*_{ae} > 0$, declining with increasing $U_r$, in a similar fashion to the case of $\zeta = 0$. The added damping ratio $\zeta_a$ compensates the structural damping ratio $-\zeta$ (dashed line), so that $\zeta_a + \zeta = 0$. Notably, $\phi_{low}$ is positive and rises with increasing $U_r$. Compared with $\zeta = 0$, it is the positive phase lag that introduces a modification in the coupling between the cylinder vibration and the fluid dynamics.

The energy $W_f$ transferred from fluid to the cylinder for each cycle of oscillation is given by

$$W_f = \int F_L \,\mathrm{d}Y = \int_t^{t+T} F_{L0} \sin(2\pi f_o t + \phi)\,\mathrm{d}(Y_0 \sin 2\pi f_o t) = \pi F_{L0} Y_0 \sin\phi. \qquad (3.21)$$

When $C_L$ leads $Y^*$ ($\phi > 0$), positive work is done on the cylinder. An increasing $\phi$ ($<90°$) provides more energy to the cylinder vibration.

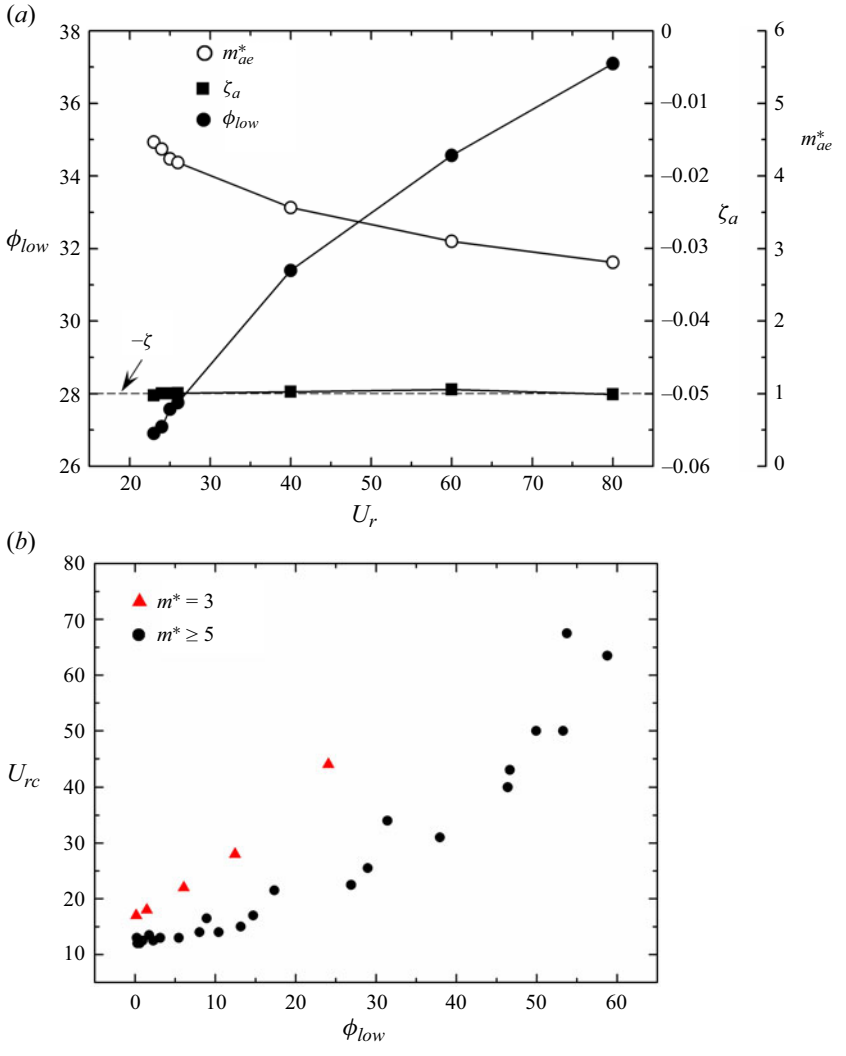


Figure 25. (*a*) Variations of phase lag $\phi_{low}$ (deg.), added damping $\zeta_a$ and effective added mass $m^*_{ae}$ with $U_r$ at $m^* = 20$ and $\zeta = 0.05$. The dashed line represents $-\zeta$. (*b*) Dependence of $U_{rc}$ on phase lag $\phi_{low}$ at the galloping onset. Here, $Re = 170$.

The presence of damping ($\zeta > 0$) introduces a positive phase lag, modifying energy transfer between the flow and cylinder, so the relationship between $U_{rc}$, $\zeta$ and $m^*$ becomes more complex and it is worth understanding the influence of $\zeta$ on galloping behaviour. The coupling in the presence of damping is crucial in determining the galloping onset, especially for lower $m^*$ ($m^* < 5$) where the role of vortex shedding becomes significant.

Figure 25(*b*) shows the dependence of $U_{rc}$ on $\phi_{low}$. At $m^* \geq 5$, a larger $\phi_{low}$ corresponds to a larger $U_{rc}$ overall. The value of $U_{rc}$ at $m^* = 3$, however, is obviously larger than that at $m^* \geq 5$, which is due to the fierce competition between SM and WM at $m^* = 3$. As discussed before, for $\zeta = 0$, $U_{rc}$ at $m^* = 3$ entirely depends on the competition between SM and WM. Therefore, for $\zeta > 0$, because of the presence of non-zero $\phi_{low}$, $U_{rc}$ at $m^* = 3$ is influenced not only by the competition but also by the magnitude of $\phi_{low}$. On the other hand, when $m^* \geq 5$, the competition is weak, with no influence on the galloping onset.

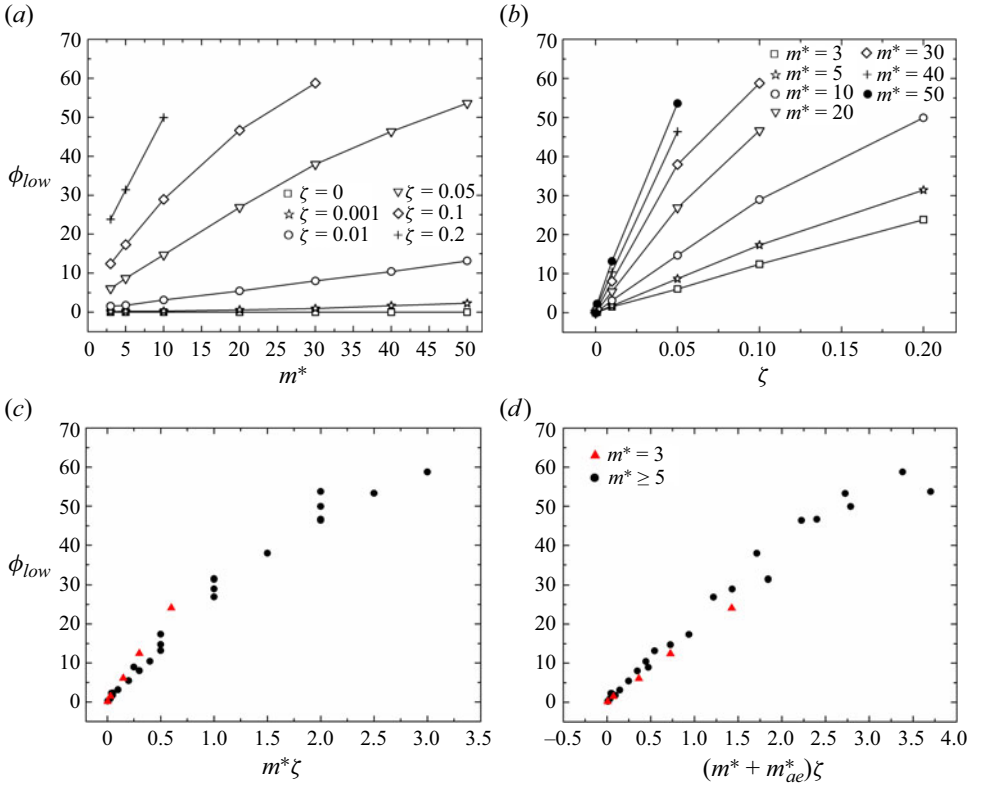


Figure 26. Effect of (*a*) mass ratio $m^*$, (*b*) damping ratio $\zeta$, (*c*) $m^*\zeta$ and (*d*) $(m^* + m^*_{ae})\zeta$ on phase lag $\phi_{low}$ at the galloping onset. Here, $Re = 170$.

The value of $U_{rc}$ is, therefore, mainly influenced by $\phi_{low}$, while a larger $m^*$ and/or $\zeta$ yields a larger $U_{rc}$.

Overall, $\phi_{low}$ being associated with work done is an important factor in determining the onset of galloping, and its magnitude is influenced by both $m^*$ and $\zeta$. Understanding the interplay between $m^*$, $\zeta$ and $\phi_{low}$ provides valuable insights into the stability of the fluid–structure system during galloping.

Figure 26(*a*,*b*) shows the effect on $\phi_{low}$ (in degrees) of $m^*$ and $\zeta$ at the onset of galloping. The relationship between $\phi_{low}$ and $m^*$ or $\zeta$ is straightforward, where $\phi_{low}$ increases with $m^*$ (figure 26*a*) and/or $\zeta$ (figure 26*b*). In the previous sections, the relationship of $U_{rc}$ with $m^*\zeta$, $(m^* + C_A)\zeta$ or $(m^* + m^*_{a0})\zeta$ has been made clear. Is there any relationship of $\phi_{low}$ with the same? Figure 26(*c*,*d*) shows the dependencies of $\phi_{low}$ on $m^*\zeta$ and $(m^* + m^*_{ae})\zeta$. It is evident that there is no clear relationship between $\phi_{low}$ and $m^*\zeta$ (figure 26*c*) or $(m^* + m^*_{ae})\zeta$ (figure 26*d*), which precludes the use of $m^*\zeta$ or $(m^* + m^*_{ae})\zeta$ to predict $\phi_{low}$ effectively. However, when $(m^* + m^*_{a0})\zeta$ is employed (figure 27), the $\phi_{low}$ data points collapse well on a line for all $m^*$ values, following a quadratic polynomial relationship between $\phi_{low}$ and $(m^* + m^*_{a0})\zeta$. This reiterates that it is $(m^* + m^*_{a0})\zeta$, not $m^*\zeta$, which intrinsically combines and reflects the mass-damping properties of the system. This relationship between $\phi_{low}$ and $(m^* + m^*_{a0})\zeta$ can be obtained as

$$\phi_{low} = -3.1[(m^* + m^*_{a0})\zeta]^2 + 28.6(m^* + m^*_{a0})\zeta. \tag{3.22}$$

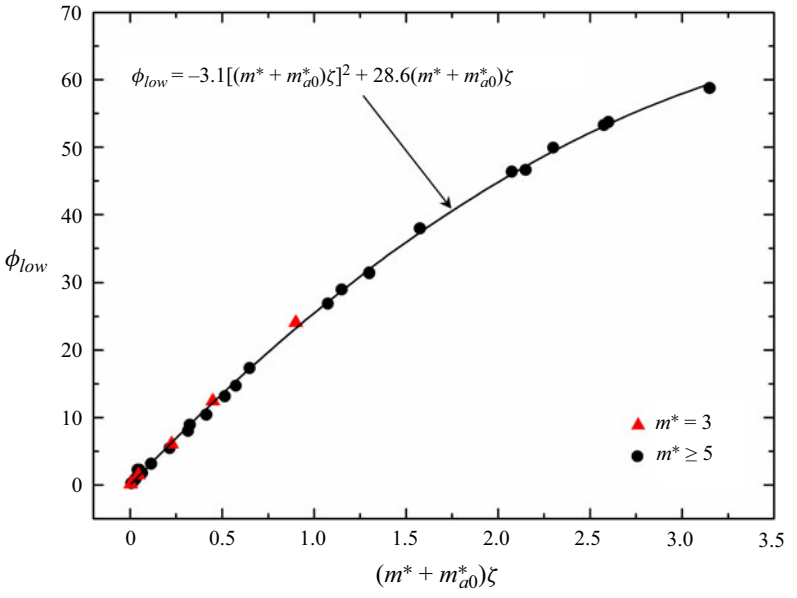


Figure 27. Effect of combined mass-damping parameter $(m^* + m^*_{a0})\zeta$ on phase lag $\phi_{low}$ at the galloping onset. Here, $Re = 170$.

This equation allows us to predict $\phi_{low}$ using the value of $(m^* + m^*_{a0})\zeta$. Parameter $m^*_{a0} = 1.5$ for a square cylinder with zero incidence angle (Chen *et al*. 2020). As long as $m^*$ and $\zeta$ are provided, we can obtain the phase lag $\phi_{low}$ between the low-pass-filtered $C_L$ and $Y^*$ at the onset of galloping.

As discussed with figure 19, the $U_{rc}$ data points collapse well on $(m^* + m^*_{ae})\zeta$ at $m^* \geq 5$, where the influence of $\phi_{low}$ is significantly greater and $U_{rc}$ is mainly determined by $\phi_{low}$. At $m^* = 3$, however, $U_{rc}$ is influenced by both the competition and the magnitude of $\phi_{low}$. As a result, $U_{rc}$ at $m^* = 3$ deviates from the fitting curve. The competition affects $U_{rc}$ at $m^* = 5$ to some degree, where $U_{rc}$ at $m^* = 5$ is 13, that is, slightly larger than 12 at $m^* \geq 10$. However, the influence of $\phi_{low}$ on $U_{rc}$ at $m^* = 5$ is greater than that at $m^* = 3$. Particularly, at $(m^* + m^*_{ae})\zeta > 0.55$, $U_{rc}$ is largely determined by $\phi_{low}$, so that the $U_{rc}$ data points fit well on a line at $m^* \geq 5$ and $(m^* + m^*_{ae})\zeta > 0.55$ (figure 19*a*). At $(m^* + m^*_{ae})\zeta \leq 0.55$, however, the $U_{rc}$ data points at $m^* \geq 5$ all lie above the fitted curve for $(m^* + m^*_{ae})\zeta > 0.55$ (figure 19*b*), as $\phi_{low}$ at $(m^* + m^*_{ae})\zeta \leq 0.55$ is not large enough to curb the mode competition.

## 4. Conclusions

Flow-induced vibrations of a square cylinder with mass ratio $m^* = 2$–$30$, damping ratio $\zeta = 0$–$1.0$ and mass-damping ratio $m^*\zeta = 0$–$50$ are numerically investigated. The investigation covers five aspects: (i) effect of $m^*$ on the vibration response, forces and frequency response, (ii) roles of effective added mass $m^*_{ae}$ in different vibration branches, (iii) characteristic changes at the borders between different branches, (iv) combined effect of $m^*$ and $\zeta$ on critical reduced velocity $U_{rc}$ and phase lag $\phi_{low}$ for galloping onset and (v) underlying mechanisms of the influences of $m^*$ and $\zeta$ on galloping.

The effect of $m^*$ is investigated on vibration responses, frequency responses, forces and effective added-mass ratio. An increase in $m^*$ reduces $U_r$ range of VIVs and advances the galloping onset. Parameter $m^*$ has distinct influences in IB, LB and GB regimes. In IB, a larger $m^*$ leads to a smaller $A^*$, $C'_L$ and $C'_{La0}$, but a larger $St$, $\bar{C}_D$ and $C'_{Lf}$. In LB,

a larger $m^*$ corresponds to a smaller $A^*$, $St$, $\bar{C}_D$, $C'_{La0}$ and $C'_{Lf}$, but a larger $C'_L$. On the other hand, in the GB regime, an increasing $m^*$ enhances $A^*$, $f_r$, $\bar{C}_D$, $C'_L$ and $C'_{Lf}$, but reduces $St$, $C'_{La0}$, $f_s/f_o$ and its gradient with $U_r$.

The effective added-mass ratio ($m^*_{ae}$) characterizes different vibration branches, being contingent on $U_r$ and $m^*$. The value of $m^*_{ae}$ in IB is positive and declines parabolically with $U_r$, which results from the fact that $f_r$ being $<1.0$ approaches 1.0. The value of $m^*_{ae}$ in LB is negative and further declines because $f_r$ being $>1.0$ shifts away from 1.0. A larger $m^*$ yields a greater $m^*_{ae}$ magnitude in both IB and LB. In GB, $m^*_{ae}$ is positive and decreases with increasing $U_r$. On the other hand, $m^*_{aes}$ is negative, yet decreasing with $U_r$. A larger $m^*$ corresponds to a smaller $m^*_{ae}$ and $m^*_{aes}$ while the effect of $m^*$ on $m^*_{aes}$ is greater than that on $m^*_{ae}$.

It is challenging to distinguish the different vibration branches. Here, several techniques are remarked upon for identifying the borders between different branches. The IB–LB boundary can be identified from the change in $m^*_{ae}$ from +ve to −ve, jumps in $St$, $\phi$ and $f_r$ or a dramatic drop in $C'_L$. On the other hand, the LB–GB boundary can be pinpointed from the change in $m^*_{ae}$ from −ve to +ve, and a jump in $C'_L$ or a drop in $f_r$.

Vibration responses undergo beating, which is linked to the difference between $f_s$ and $3f_o$ or $5f_o$, with a beating frequency of $|f_s - 3f_o|$ or $|f_s - 5f_o|$. The beating amplitude in $Y^*$ or $C_L$ grows when $f_s/f_o$ approaches $f_s/f_o = 3$ or 5 but declines when $f_s/f_o$ departs from $f_s/f_o = 3$ or 5. The beating phenomenon of a square cylinder in GB is derived from the modulation between $f_s$ and $(2n+1)f_o$, where $n = 1, 2, \ldots$, not directly caused by the difference between $f_s$ and $f_o$.

Effects of $m^*$, $\zeta$, $m^*\zeta$, $(m^* + m^*_{a0})\zeta$ and $(m^* + m^*_{ae})\zeta$ on $U_{rc}$ and $\phi_{low}$ for galloping onset are revealed at $U_r = 1$–80. Parameter $m^*$ has a negligible influence on $U_{rc}$ for $\zeta \leq 0.01$. This is, nevertheless, not the case for $\zeta > 0.01$ where $U_{rc}$ adjourns with increasing $m^*$ and/or $\zeta$. The competition between vortex shedding associated with low-frequency vibration (SM) and high-frequency vibration (WM) determines $U_{rc}$ at low $m^*$ ($=3$) as does $\phi_{low}$ at a large $m^* \geq 5$. Term $(m^* + m^*_{a0})\zeta$ successfully collapses all $\phi_{low}$ data on a line for all $m^*$ and $\zeta$ values, with a quadratic polynomial relationship between $\phi_{low}$ and $(m^* + m^*_{a0})\zeta$. Similarly, $U_{rc}$ data fit well on $(m^* + m^*_{ae})\zeta$ at $m^* \geq 5$, where $U_{rc}$ grows linearly with increasing $(m^* + m^*_{ae})\zeta$. Term $m^*\zeta$ as well as $(m^* + m^*_{a0})\zeta$ or $(m^* + C_A)\zeta$ does not serve well to characterize a fluid–structure system. We introduce a combined mass-damping parameter $(m^* + m^*_{ae})\zeta$ that serves as the unique criterion to predict the galloping onset. This indicates that $(m^* + m^*_{ae})\zeta$ works well to represent the property of a fluid–structure system.

**Acknowledgements.** The authors wish to acknowledge the support given by the National Natural Science Foundation of China through grant 11672096 and by the Research Grant Council of Shenzhen Government through grant JCYJ20180306171921088.

**Declaration of interests.** The authors report no conflict of interest.

**Author ORCIDs.**
Cuiting Lin https://orcid.org/0000-0002-2490-5504;
Md. Mahbub Alam https://orcid.org/0000-0001-7937-8556.

## References

ALAM, M.M. 2021 Effects of mass and damping on flow-induced vibration of a cylinder interacting with the wake of another cylinder at high reduced velocities. *Energies* **14**, 5148.

ALAM, M.M. 2022 A note on flow-induced force measurement of oscillating cylinder by loadcell. *Ocean Engng* **245**, 110538.
BAHMANI, M.H. & AKBARI, M.H. 2010 Effects of mass and damping ratios on VIV of a circular cylinder. *Ocean Engng* **37**, 511–519.
BARRERO-GIL, A., SANZ-ANDRES, A. & ROURA, M. 2009 Transverse galloping at low Reynolds numbers. *J. Fluids Struct.* **25**, 1236–1242.
BEARMAN, P.W. 1984 Vortex shedding from oscillating bluff bodies. *Annu. Rev. Fluid Mech.* **16**, 195–222.
BHATT, R. & ALAM, M.M. 2018 Vibrations of a square cylinder submerged in a wake. *J. Fluids Mech.* **853**, 301–332.
BLEVINS, R.D. 1990 *Flow-induced Vibration*. Van Nostrand Reinhold.
BLEVINS, R.D. & COUGHRAN, C.S. 2009 Experimental investigation of vortex-induced vibration in one and two dimensions with variable mass, damping, and Reynolds number. *J. Fluids Engng* **131**, 101202.
CHEN, G., ALAM, M.M. & ZHOU, Y. 2020 Dependence of added mass on cylinder cross sectional geometry and orientation. *J. Fluid Struct.* **99**, 103142.
DANIEL, W.C., TODD, M.C. & YAHYA, M.S. 2021 Flow-induced vibrations of a square prism free to oscillate in the cross-flow and inline directions. *J. Fluid Mech.* **919** (A2), 1–31.
GOVARDHAN, R. & WILLIAMSON, C.H.K. 2000 Modes of vortex formation and frequency response of a freely vibrating cylinder. *J. Fluid Mech.* **420**, 85–130.
GOVARDHAN, R. & WILLIAMSON, C.H.K. 2004 Critical mass in vortex-induced vibration of a cylinder. *Eur. J. Mech. (*B*/Fluids)* **23**, 17–27.
GRIFFIN, O.M. 1980 Vortex-excited cross-flow vibrations of a single cylindrical tube. *Trans ASME: J. Press. Vessel Technol.* **102**, 158–166.
GRIFFIN, O.M., SKOP, R.A. & RAMBERG, S.E. 1975 The resonant vortex-excited vibrations of structures and cable systems. In *7th Offshore Technology Conference, Houston, TX*, OTC Paper 2319.
HAN, P. & LANGRE, E.D. 2022 There is no critical mass ratio for galloping of a square cylinder under flow. *J. Fluid Mech.* **931**, A27 (1–20).
JOLY, A., ETIENNE, S. & PELLETIER, D. 2012 Galloping of square cylinders in cross-flow at low Reynolds numbers. *J. Fluids Struct.* **28**, 232–243.
KHALAK, A. & WILLIAMSON, C.H.K. 1999 Motions, forces and mode transitions in vortex-induced vibrations at low mass-damping. *J. Fluids Struct.* **13**, 813–851.
LI, X., LYU, Z., KOU, J. & ZHANG, W. 2019 Mode competition in galloping of a square cylinder at low Reynolds number. *J. Fluid Mech.* **867**, 516–555.
LIGHTHILL, J 1986 Wave loading on offshore structures. *J. Fluid Mech.* **173**, 667–681.
MANSON, J.R., PENDER, G. & WALLIS, S.G. 1996 Limitations of traditional finite volume discretizations for unsteady computational fluid dynamics. *AIAA J.* **34** (5), 1074–1076.
MELIGA, P. & CHOMAZ, J. 2011 An asymptotic expansion for the vortex-induced vibrations of a circular cylinder. *J. Fluid Mech.* **671**, 137–167.
MITTAL, N.S. 2017 A new regime of multiple states in free vibration of a cylinder at low *Re*. *J. Fluids Struct.* **68**, 310–321.
PAÏDOUSSIS, M.P., PRICE, S.J. & DELANGRE, E. 2010 *Fluid-Structure Interactions: Cross-Flow-Induced Instabilities*. Cambridge University Press.
PAN, Z.Y., CUI, W.C. & MIAO, Q.M. 2007 Numerical simulation of vortex-induced vibration of a circular cylinder at low mass-damping using RANS code. *J. Fluid Struct.* **23**, 23–27.
PATANKAR, S.V. 1980 *Numerical Heat Transfer and Fluid Flow*. Hemisphere Publishing, Taylor & Francis Group.
QIN, B., ALAM, M.M. & ZHOU, Y. 2017 Two tandem cylinders of different diameters in crossflow: flow-induced vibration. *J. Fluid Mech.* **829**, 621–658.
QIN, B., ALAM, M.M. & ZHOU, Y. 2019 Free vibrations of two tandem elastically mounted cylinders in cross-flow. *J. Fluid Mech.* **861**, 349–381.
RABIEE, A.H. & FARAHANI, S.D. 2020 A comprehensive study of heat transfer characteristic and two-dimensional FIV for heated square-section cylinder with different damping ratios. *Intl Commun Heat Mass Transfer* **116**, 104680.
SARPKAYA, T. 1978 Fluid forces on oscillating cylinders. *ASCE J. Waterway Port Coaast. Ocean Div.* **104**, 275–290.
SARPKAYA, T. 1995 Hydrodynamic damping, flow-induced oscillation, and biharmonic response. *ASME J. Offshore Mech. Arctic Engng* **117**, 232–238.
SEN, S. & MITTAL, S. 2011 Free vibration of a square cylinder at low Reynolds numbers. *J. Fluids Struct.* **27**, 875–884.

SEN, S. & MITTAL, S. 2015 Effect of mass ratio on free vibrations of a square cylinder at low Reynolds numbers. *J. Fluids Struct.* **54**, 661–678.

SEN, S. & MITTAL, S. 2016 Free vibrations of a square cylinder of varying mass ratios. *Procedia Engng* **144**, 34–42.

SHAABAN, M. & MOHANY, A. 2018 Flow-induced vibration of three unevenly spaced in-line cylinders in cross-flow. *J. Fluids Struct.* **76**, 367–383.

SHEN, L.W., CHAN, E.S. & WEI, Y. 2018 Beating motion of a circular cylinder in vortex-induced vibrations. *Fluid Dyn. Res.* **50**, 025503.

SOURAV, K. & SEN S. 2019 Transition of VIV-only motion of a square cylinder to combined VIV and galloping at low Reynolds numbers. *Ocean Engng* **187**, 106208.

VOORHEES, A., DONG, P., ATSAVAPRANEE, P., BENAROYA, H. & WEI, T. 2008 Beating of a circular cylinder mounted as an inverted pendulum. *J. Fluid Mech.* **610**, 217–247.

WILLIAMSON, C.H.K. & GOVERDHAN, R. 2004 Vortex-induced vibrations. *Annu. Rev. Fluid Mech.* **36**, 413–455.

YAO, W. & JAIMAN, R.K. 2017 Model reduction and mechanism for the vortex-induced vibrations of bluff bodies. *J. Fluid Mech.* **827**, 357–393.

ZHANG, W., LI, X., YE, Z. & JIANG, Y. 2015 Mechanism of frequency lock-in in vortex-induced vibrations at low Reynolds numbers. *J. Fluid Mech.* **783**, 72–102.

ZHAO, J., LEONTINI, J., JACONO, D.L. & SHERIDAN, J. 2019 The effect of mass ratio on the structural response of a freely vibration square cylinder oriented at different angles of attack. *J. Fluids Struct.* **86**, 200–212.

ZHAO, J., LEONTINI, J.S., JACONO, D.L. & SHERIDAN, J. 2014 Fluid-structure interaction of a square cylinder at different angles of attack. *J. Fluid Mech.* **747**, 688–721.

ZHAO, M. 2015 Flow-induced vibrations of square and rectangular cylinders at low Reynolds number. *Fluid Dyn. Res.* **47**, 025502.

ZHENG, Q. & ALAM, M.M. 2017 Intrinsic features of flow past three square prisms in side-by-side arrangement. *J. Fluid Mech.* **826**, 996–1033.